CHAPTER 4

Effect of Stress-Dependent Permeability, Ramp Loading, and Non-Darcian Flow on Saturated Consolidation

4.1 INTRODUCTION

In the previous chapter, it is assumed that the permeability and compressibility of the soil remain constant throughout the consolidation process. This assumption simplifies the solution for practical applications and makes it readily solvable. However, this assumption has led to results that significantly diverge from experimental data, rendering them unsuitable for solving field problems. Various approaches have contributed to this hypothesis by considering a linear variation of e-log$k$ and e-logσ', making effective stress the governing criterion for consolidation. One of the idealizations considered in the classical 1D consolidation theory, regarding the constancy of flow and deformation characteristics, was rigorously verified by several researchers (Burland 1990; Hai and Chen 2013; Li et al. 2018; Zhuang and Xie 2005a, Zhuang and Xie 2005b Poskitt 1969 ,Mesri and Rokhsar 1974 Lekha et al. 2003 Geng et al. 2006 Abbasi et al. 2007 Naga and Pender 2012) in the last few decades. These works were carried out by considering the influence of effective stresses on the permeability and the compressibility values; nevertheless, the spatial gradient of the permeability was taken to be zero, resulting in *quasi-permeability* variation. This approach faces limitations in the consolidation equation if the slopes of the of e-log$k$ and e-logσ' curves are equal, as permeability in this scenario does not depend on effective stress (Abbasi et al., 2007).

Furthermore, the available literature also suggests that the linear relationship between velocity and hydraulic gradient (Swartzendruber 1962; Elnaggar et al. 1973; Pascal et al. 1981; Olsen 19865; Olsen 1985; Hansbo 2003; Singh and Chakraborty 2022) does not model the fine-grained clays suitably. This can be attributed to the presence of a relatively lower hydraulic gradient in fine-grained soils. Results obtained from laboratory experiments and field observation indicate that an exponential correlation exhibited between flow velocity (v) and hydraulic gradient (i) up to a specific point (critical hydraulic gradient, i_1), and beyond that, it conforms to a linear trend. The reason can be attributed to the fact that the texture and electrical force field within the clay particles influences the movement of the water largely under the low hydraulic gradient (Hansbo, 2003). A number of studies (Dubin and Moulin 1986; Ing and Xiaoyan 2002; Xie et al. 2007; Liu et al. 2009; Li et al. 2010,2012; Li and Xie, 2013) were carried out to estimate the consolidation behavior of soft clays by considering the non-Darcian flow, based on the exponent and threshold gradient. Current literature lacks studies that comprehensively address the impact of stress-dependent parameters (permeability and compressibility), non-Darcian flow laws, and time-varying ramp loading on the consolidation settlement of clays. This motivates the present research.

The first section of this chapter deals with the impact of quasi-permeability and total permeability on the rate of consolidation under constant loading, with the flow of water governed by Darcy's law. Two models are employed to explore the influence of various soil parameters and ultimate load (q) on the consolidation phenomenon: Case A, representing quasi-permeability variation, and Case B, representing total permeability variation (where the spatial gradient of permeability is not assumed to be zero). The second part of this chapter simultaneously accounts for the (a) spatial and stress gradient of the permeability function, (b) exponential and threshold gradient-based non-Darcian flow

behaviour (Elnaggar et al.1973), and (c) time-dependent (ramp) loading. Two cases are considered - Case A, representing total permeability variation, and Case B, representing constant permeability but variable compressibility.

4.2 INVESTIGATING THE EFFECT OF QUASI AND TOTAL PERMEABILITY VARIATION

4.2.1 Problem Statement

An isotropic, saturated clay layer of thickness, *H*, is subjected to a constant load, *q*, as shown in Fig. 4.1a. The permeability and the compressibility parameters are stress-dependent. During the consolidation, as the excess pore water pressure (PWP) dissipates with time, the effective stress ($\sigma'(z,t)$) changes with time and space. The change in $\sigma'(z,t)$ causes the variation in the void ratio and subsequently impacts the water flow rate. Thus, the permeability (*k*), which depends on effective stress, becomes functional. Traditionally, the literature on consolidation with the nonlinear material properties considers the variation of permeability with σ' but not with *z*; this variation is regarded as the *quasi-permeability variation*, wherein, $\partial k / \partial z$ is enforced to zero. The first section of this chapter investigates the difference in the consolidation behavior if, along with the stress gradient, the spatial gradient of permeability is also taken to be non-zero. The existence of $\partial k / \partial z$ and $\partial k / \partial \sigma'$ is termed here as the *total-permeability variation*. In this context, it is to be noted that the heterogeneity of the considered domain is not inherent, but stress-induced. The analyses are to be performed for PTPB and PTIB drainage boundaries.

4.2.1.1 Stress-Dependent Characteristics

The permeability and compressibility characteristics are governed by the logarithmic relationship:

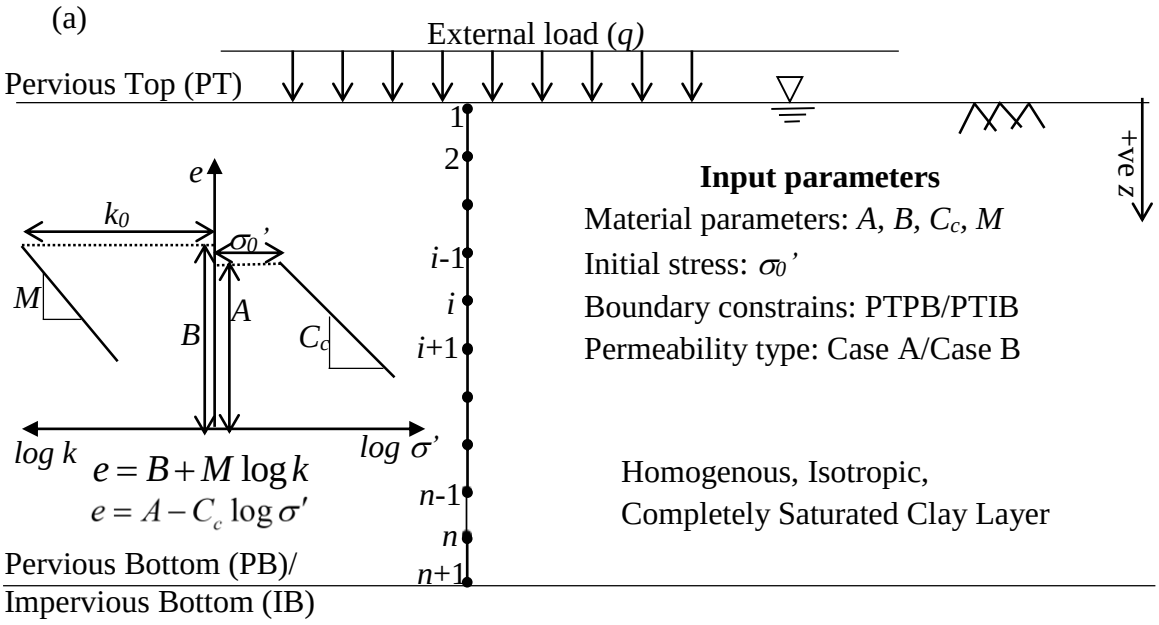

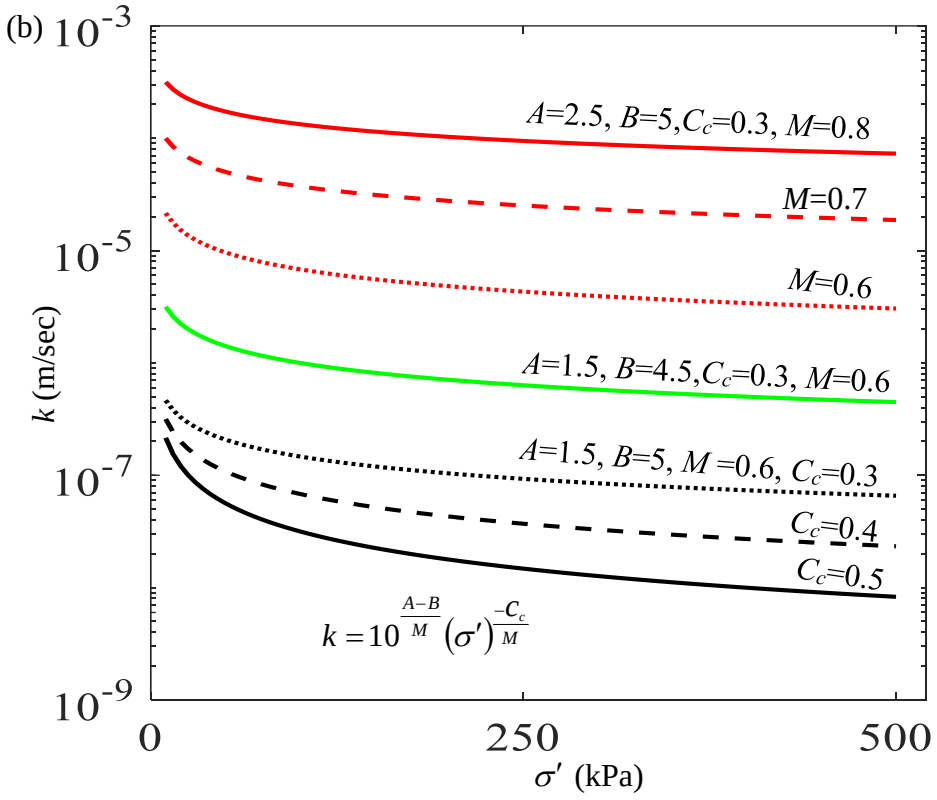

Fig. 4.1 (a) A schematic diagram of the problem statement, ramp loading applied (b)impact of various soil parameter on stress-dependent permeability.

$e-\sigma'$ relationship: $e = A - C_c \log \sigma'$ (4.1a)

e–k relationship: $e = B + M \log k$ (4.1b)

A and B indicate the intercept on the void ratio line corresponding to unit effective stress (σ'=1 kPa) and unit permeability (k=1 m/sec), respectively. The parameters M and C_c are the slope of e–log$k$ and e–logσ' curves, respectively; M= permeability index and C_c = compressibility index.

Combining Eqs. 4.1a and 4.1b, the $k-\sigma'$ relationship can be written as:

$$k = 10^{\frac{A-B}{M}} (\sigma')^{-\frac{C_c}{M}}. \quad (4.2)$$

Fig. 4.1b shows the nonlinear variation of permeability with the induced vertical effective stress. For realistic values of the permeability, A must be less than B. At any location, for the developed effective stress, the permeability reduces with the (i) increase in B and C_c values and (ii) decrease in A and M values.

4.2.2 Forms of the governing differential equations (GDE)

The 1-D diffusion equation is formulated by considering the (a) continuity equation, (b) Darcy's linear flow relationship, (c) compressibility-based stress-dependent permeability factor, (d) non-zero divergence of the flow vector, and (e) fundamental principle that the change in pore water pressure (u) equal to the change in effective stress. The steps for determining the governing differential equations are cited in Appendix B1. Two different cases are considered during the development of the formulations. They are:

Case A (Quasi-Permeability variation): the spatial gradient of the permeability is zero

Case B (Total-Permeability variation): the spatial gradient of the permeability is non-zero

The parabolic partial differential equations (PDE) obtained for these two cases are written below:

$$\text{Case A}: X_1 \frac{\partial^2 u}{\partial z^2} = \frac{\partial u}{\partial t} \tag{4.3}$$

$$\text{Case B}: X_1 \frac{\partial^2 u}{\partial z^2} + Y_1 \frac{\partial u}{\partial z} = \frac{\partial u}{\partial t} \tag{4.4}$$

$$\text{Where } C_n = \frac{2.3(1+e_0)10^{\frac{A-B}{M}}}{C_c \gamma_w};\ X_1 = C_n(\sigma')^{\beta};\ Y_1 = C_n \gamma_w (1-\beta)(\sigma')^{\beta-1} i;\ \beta = 1 - C_c/M$$

$$X_1 = \underbrace{2.3\sigma'(1+e_0)/(C_C \gamma_W)}_{\substack{\text{Compressibility} \\ \text{Characteristics}}} \cdot \underbrace{10^{(A-B)/M} \cdot (\sigma')^{\beta-1}}_{\substack{\text{Permeability} \\ \text{Characteristics}}} \tag{4.5}$$

In both cases, the spatial derivatives (on the left-hand side) are equated with the temporal derivative on the right-hand side. The parameter X_1 consists of two terms: (a) constant term, C_n, and (b) resulting effective stress (σ'), whereas, the parameter Y_1 consists of three terms: (a) C_n, (b) σ', and (c) hydraulic gradient (i). The dimensions of X_1 and Y_1 are L^2T^{-1} and LT^{-1}, respectively. Case A is a special case of the generalized Case B, wherein the permeability does not vary in spatial direction so Y_1 is considered to be zero. The exponent parameter (dimensionless), β, which is associated with the effective stress, depends on the ratio of C_c/M. A few researchers (Geng et al., 2006; Lekha et al., 2003) had earlier described the impact of C_c/M on the consolidation process. The equation representing Case A resembles the conventional dissipation equation ($c_v u'' = \dot{u}$); the only difference is the coefficient (X) term, which is a function of σ'. If C_c/M =1, X becomes a constant number, C_n. This indicates that the conventional diffusion equation is the quasi-permeability variation with C_c=M. On the contrary, Case B demonstrates that permeability depends on effective stress for all values of C_c/M.

4.2.3 Numerical Scheme

The Crank-Nicolson implicit scheme of the finite difference method is utilized to solve the initial value problem (IVP), represented by the governing differential equation along with the boundary and initial conditions. The domain in the vertical direction is discretized into *n* equally-spaced segments, resulting in *n*+1 number of grid points, as shown in Fig. 4.1a. For any arbitrary i^{th} grid point, the discretized equation is as follows:

Case A
$$X_{1@i}\left[\frac{1}{2}\left\{\left.\frac{\partial^2 u}{\partial z^2}\right|_i^{t+\Delta t}+\left.\frac{\partial^2 u}{\partial z^2}\right|_i^{t}\right\}\right]=\left.\frac{\partial u}{\partial t}\right|_i \tag{4.6}$$

Case B
$$X_{1@i}\left[\frac{1}{2}\left\{\left.\frac{\partial^2 u}{\partial z^2}\right|_i^{t+\Delta t}+\left.\frac{\partial^2 u}{\partial z^2}\right|_i^{t}\right\}\right]+Y_{1@i}\left\{\left.\frac{\partial u}{\partial z}\right|_i^{t+\Delta t}\right\}=\left.\frac{\partial u}{\partial t}\right|_i \tag{4.7}$$

Appendix B2 shows the process of discretization and the algebraic equations obtained thereof. To linearize the nonlinear equations, the spatial gradient terms involved in Y_1 are taken at the previous (known) time step. Thus, the equation can be converted into a simultaneous set of linear algebraic equations ($G\times U^{t+\Delta t}=H^t$). The equations are solved by employing the Gauss elimination technique.

At the preliminary stage, the homogenous compressible clays are first assigned with a uniform initial effective stress σ_0', distinct *e*–log*k*, *e*–logσ'. Hence, the input parameters for this problem are (i) initial vertical effective stress (σ_0'), (ii) permeability characteristics (*A*, *M*), (iii) compressibility characteristics (*B*, C_c), (iv) unit weight of water (γ_w). Thereafter, on the basis of e_0 and *e*–log*k* curves, k_0 is calculated. At the instant of load application, all the grid points are assigned with the uniform values of e_0 and k_0. With the advancement in consolidation, the effective stress changes, resulting in a change in the void ratio and a consequent variation in permeability at different locations. Fig. 4.2 presents the combined representation of the linear profiles to illustrate the process of evaluating the

permeability for a specific vertical effective stress. The flowchart of the problem is presented in Fig. 4.3. The entire numerical program is developed in *MATLAB* (version 2018) tool.

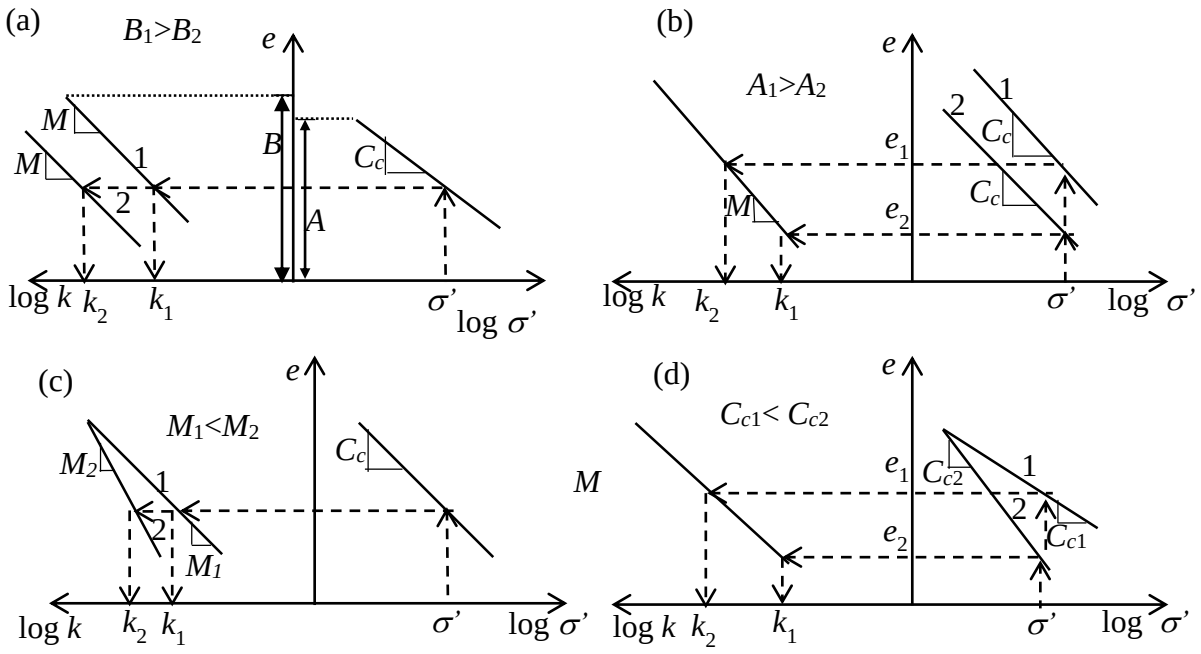

Fig. 4.2 Relation between *e-logσ'-logk* on logarithmic scale with (a) variation of *M* and *B* (b) variation of C_C and *A.*

4.2.4 Results and Discussions

Following Abbasi et al. (2007), the parameters chosen in the analysis are shown in Table 4.1. In the present analysis, the parameter C_n is taken to be 0.0019 (this value is computed from Eq. 4.5 by using the constant parameters provided in the table). With the increase in β, the initial (k_0) and final (k_f) permeabilities rise by an order of 2. However, the range between k_0 and k_f decreases with increasing β. The excess pore water pressure, u are computed at each node with the advancement in the dissipation process. Results are presented in the form of normalized isochrones and U_{avg} curve. The impact of C_c/M and external load q on consolidation process are critically analysed.

Table 4.1 Specification of the sample

Constant Parameters	C_c/M	M	β $(1-C_c/M)$	k_0 (*m/sec*)	k_f (*m/sec*)	Δk in %
A=3, B=5, C_c=0.6, e_0=2.58, σ'_0=5kPa, e_f=1.79, C_n=0.0019*	1.50	0.40	–0.50	8.9443e-07	9.2943e-09	98.96
	1.25	0.48	–0.25	9.1121e-06	2.0270e-07	97.78
	1.00	0.60	0.00	9.2832e-05	4.4206e-06	95.24
	0.75	0.80	0.25	9.4574e-04	9.6407e-05	89.81
	0.50	1.20	0.50	9.6210e-03	2.1256e-03	77.91

* Corresponding to M=0.7

4.2.4.1 Influence of C_c/M on consolidation behaviour

The soil's stiffness and permeability at any given moment are influenced by the soil state parameters C_c and M. A higher C_c value implies greater deformability but delayed consolidation; on the contrary, the higher the M the faster the consolidation. This section verifies the ratio of the compressibility and permeability indices on the consolidation behaviour. The impact of C_c/M is verified on the (a) isochrone curves (Fig. 4.4), (b) U_{avg} vs T_n curves (Fig. 4.5), and (c) temporal variation of the PWP profiles (Fig. 4.6) at the center of the consolidating layer; where, $T_n(\text{time factor}) = C_n\left(\sigma'\right)^{\beta} \cdot t \big/ D_p^2$. Five different C_c/M ratios (=0.5, 0.75, 1, 1.25, and 1.5) are considered. For Case A, if C_c/M = 1, Eq. 4.3 becomes stress-independent and takes the form of the conventional diffusion equation (Terzaghi, 1925). For C_c/M smaller than 1, faster consolidation is observed, while for C_c/M greater than 1, the consolidation process is slower (Lekha, Krishnaswamy and Basak, 2003; Zhuang, Xie and Li, 2005; Abbasi *et al.*, 2007). The solid lines represent the Case A model, the dashed lines correspond to the Case B model, and the dotted lines depict the ideal condition based on Terzaghi's equation.

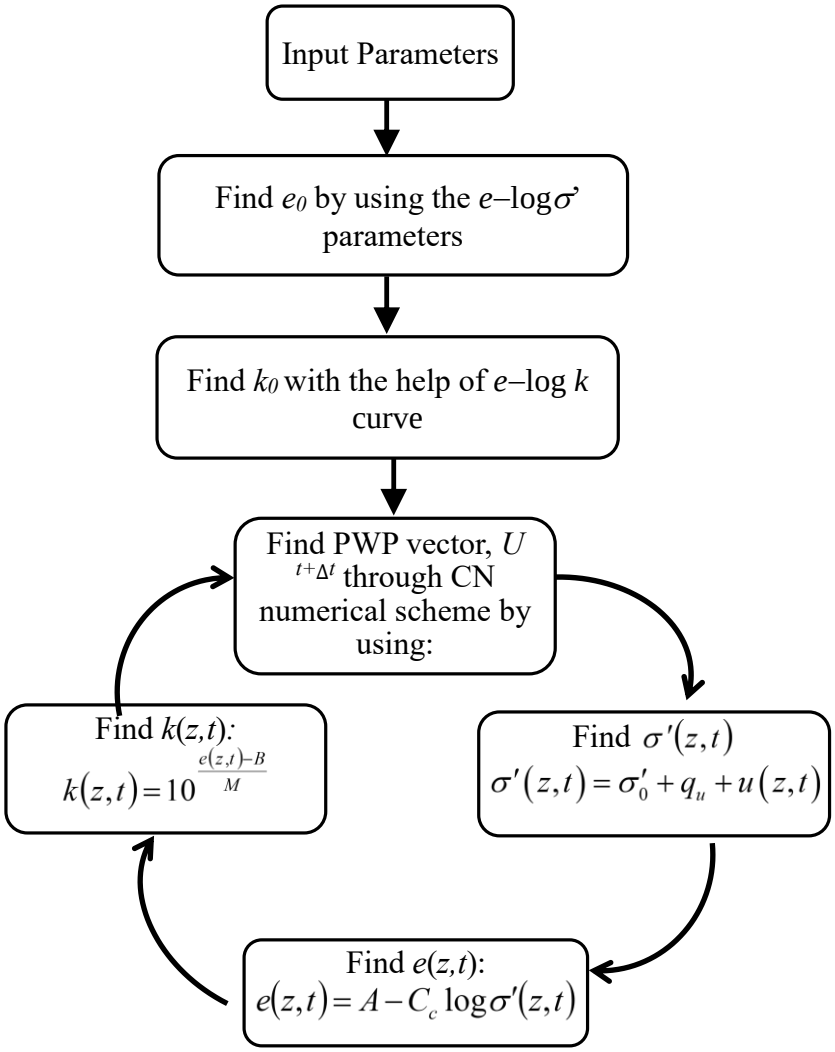

Fig 4.3 Flow chart of the steps for consolidation

Fig. 4.4 displays the normalized isochrones drawn at T_n=0.2 and q=100kpa for various C_c/M ratios and different drainage boundary conditions. Fig 4.4 indicates that under PTPB, the pore water pressure (PWP) is zero at both boundaries. Conversely, for PTIB, the isochrones intersect the bottom surface orthogonally. As the C_c/M ratio increases, the rate of consolidation decreases. Irrespective of the drainage boundaries, the discrepancy in the area enclosed by successive isochrones continues to grow as C_c/M decreases. It can also be observed that the enlargement in the enclosed area further grows for Case A than Case B.

Fig 4.5 shows the global view of consolidation through the U_{avg} vs T_n graphs and Fig. 4.6 shows the temporal variation of PWP at the mid-depth of the clayey layer.

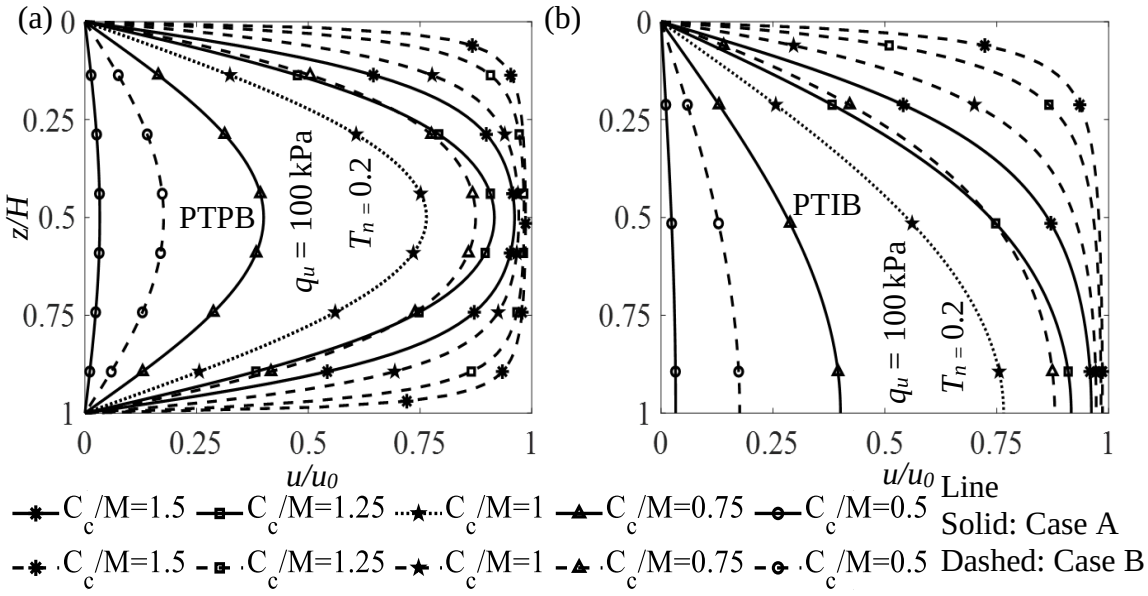

Fig. 4.4 Normalised isochrones for (a) PTPB condition (b) PTIB condition at T_n=0.2

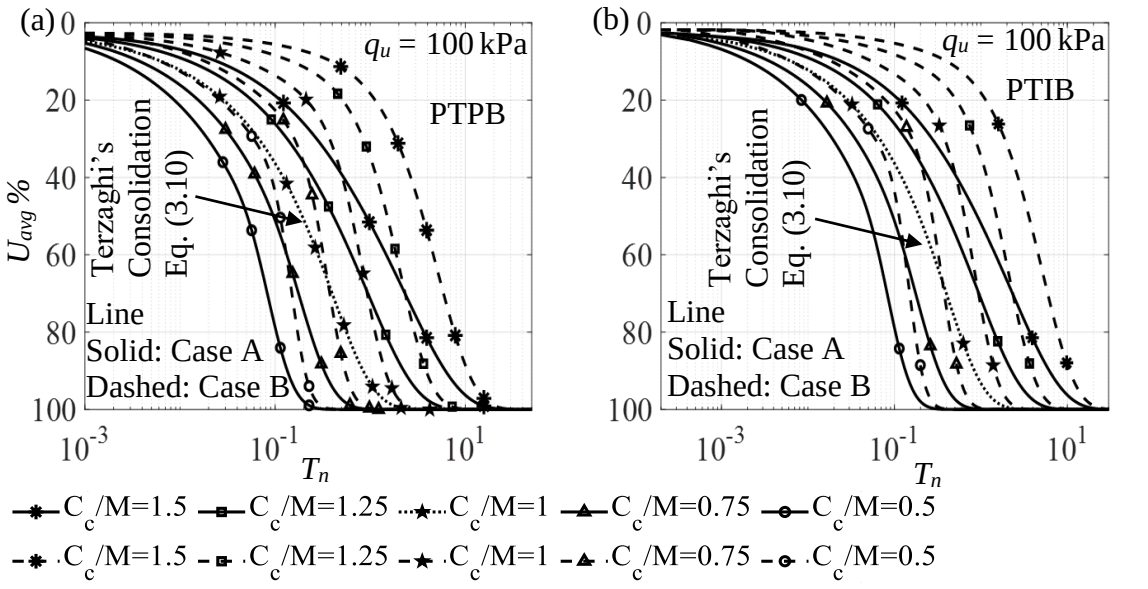

Fig. 4.5 U_{avg} vs t_n for (a) PTPB condition (b) PTIB condition

The impact of C_c/M was observed to exhibit a similar outcome in both Cases A and B. An increase in C_c/M value is associated with a decrease in dissipation rate. This can be attributed to the fact that higher C_c/M leads towards the reduction in β and, consequently, reduces the effective stress term. The reduced value of β and effective stress directly influences the stress-dependent coefficient of consolidation. The rate of dissipation is much

slower for Case B in the initial stage of consolidation. One interesting fact that needs to be highlighted is that although the consolidating curves corresponding to Cases A and B manifest an appreciable gap between them, say up to 30%-35% nevertheless, this gap shrinks, and 100% consolidation for Cases A and B is achieved almost at the same time. It can be interpreted that Case A, featuring quasi-permeability variation, achieves a certain level of consolidation in a significantly shorter time compared to Case B, while the maximum consolidation is achieved in nearly the same time frame. It shows that the speed of consolidation accelerates for Case B after attaining a certain percentage of consolidation. The consolidating curves for Case B with negative β deviates considerably from the traditional U_{avg} vs T_v curves.

4.2.4.2 Effect of *q* on consolidation behaviour

The effective stress in the soil is influenced by the ultimate load, leading to variations in the coefficient of consolidation over time and depth, ultimately impacting soil consolidation. Additionally, alterations in the C_c/M ratio result in different effects on the consolidation curve for each load increment. Fig. 4.7 illustrates the impact of q under different C_c/M ratios, specifically 0.5 and 1.5, for both PTPB and PTIB boundary conditions. This can be explained by the increase in applied stress leading to a rise in effective stress for successive intervals. Fig. 4.8 displays the spatial variation of C_n/X_1, for different q values specifically 50, 100, 150, and 200, corresponding to both Case A and Case B under PTPB and PTIB conditions. Observing Fig 4.8, it is evident that with an increase in the value of q, the differences between successive lines representing the distinctions between Case A and Case B decrease. This suggests a minimal difference in the coefficient of consolidation values, implying that at very high loads, Case A and Case B yield similar results, while the difference is more significant at lower loads. The impact of load is more pronounced when $C_c/M < 1$.

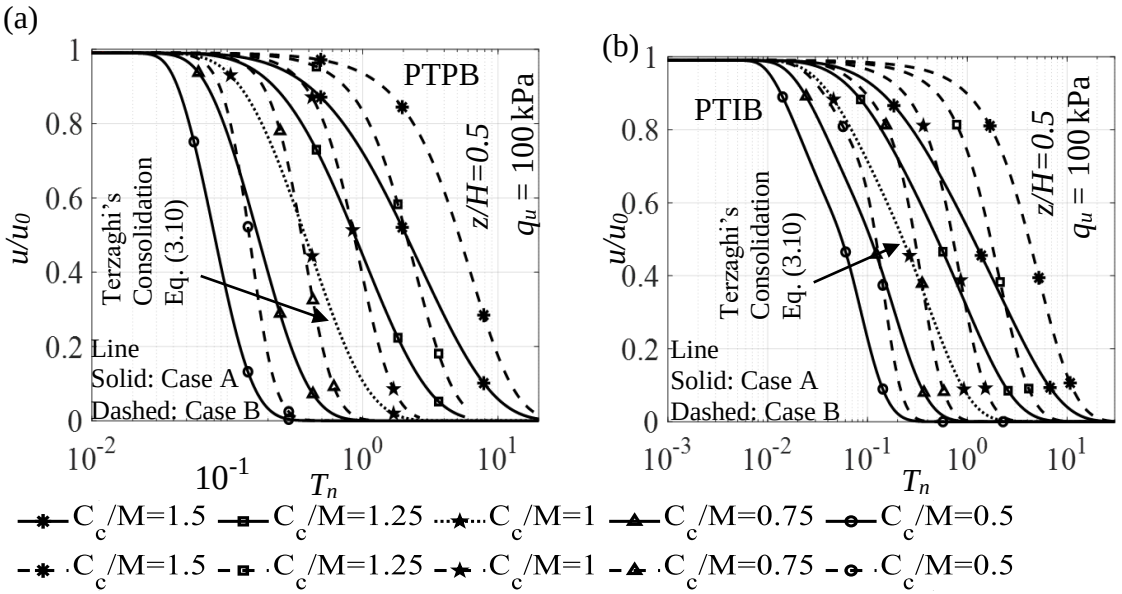

Fig. 4.6 u/u_0 vs T_n at mid-depth for (a) PTPB condition (b) PTIB condition

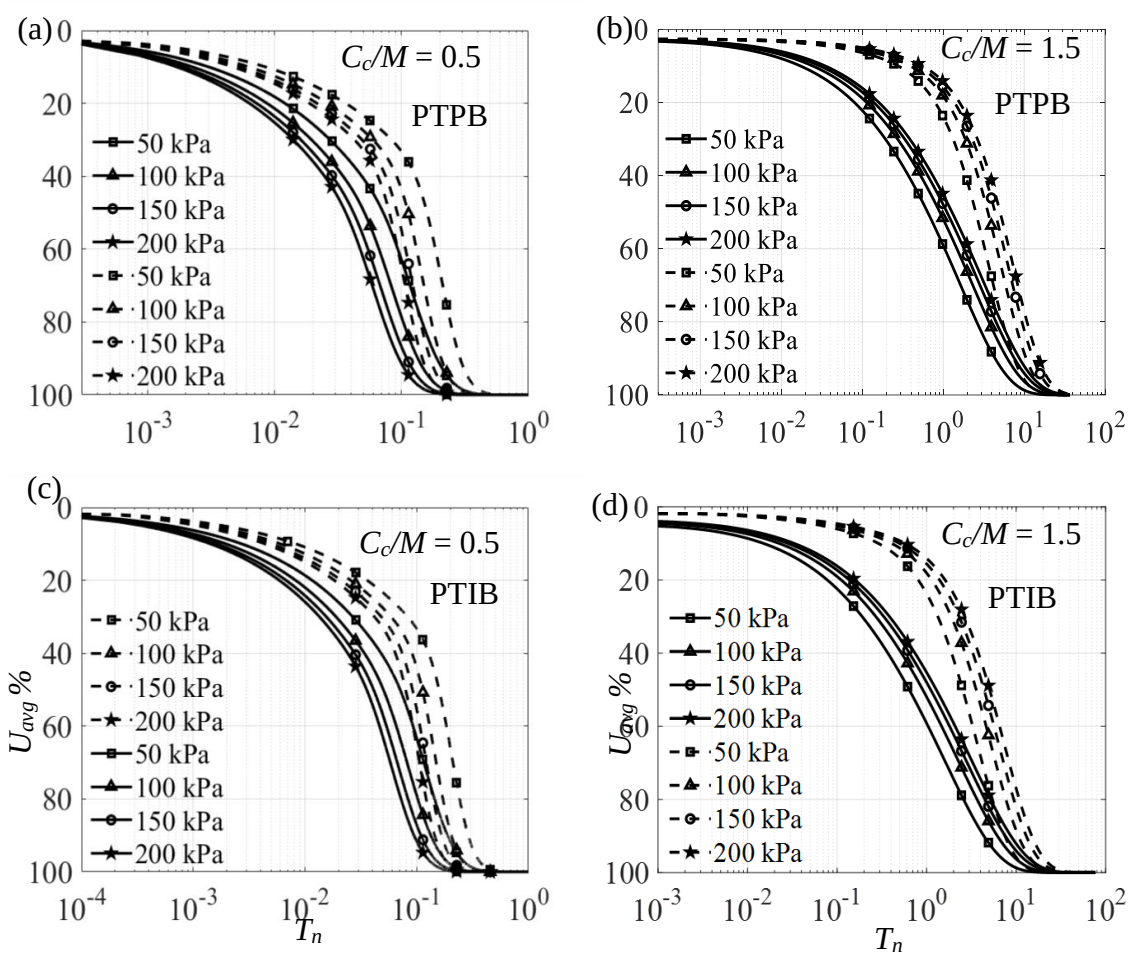

Note : Solid Line: Case A; Dashed Line: Case B

Fig. 4.7. Effect of loading for (a) C_c/M = 0.5 in PTPB drainage condition (b) C_c/M =1.5 in PTPB drainage condition (c) C_c/M = 0.5 in PTIB drainage condition (d) C_c/M =1.5 in PTIB drainage condition

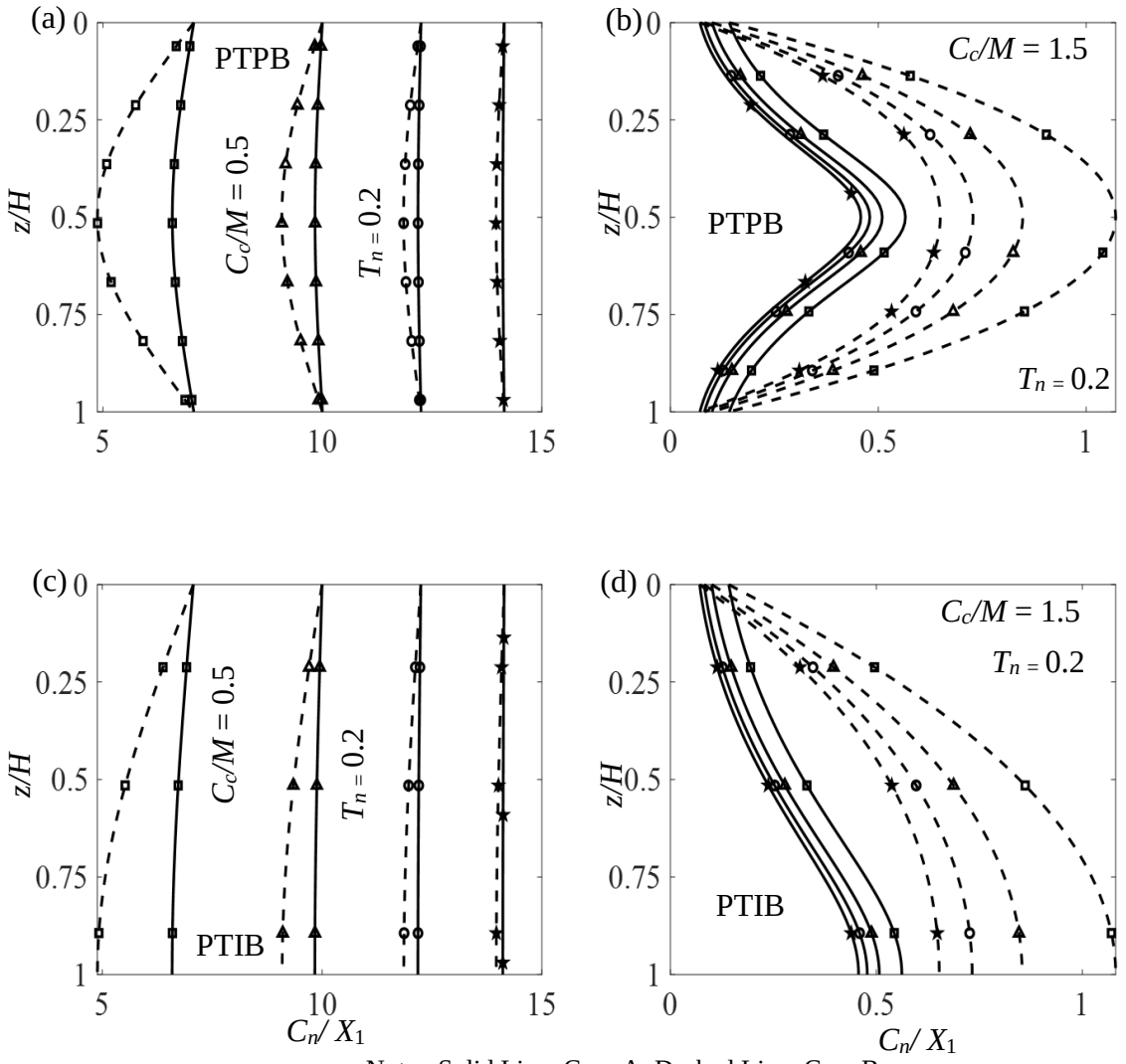

Fig. 4.8 Effect of loading on C_n/X_1 for (a) C_c/M = 0.5 in PTPB drainage condition (b) C_c/M =1.5 in PTPB drainage condition (c) C_c/M = 0.5 in PTIB drainage condition (d) C_c/M =1.5 in PTIB drainage condition

4.3 IMPACT OF NON-DARCIAN FLOW RULE AND RAMP LOADING

4.3.1 Problem Statement

A homogenous, isotropic, normally consolidated, and saturated clay layer of thickness, H, is subjected to a time-dependent external (ramp) loading $q(t)$. The loading can be expressed as under:

$$q(t) = q_u\,(t/t_c) \quad \text{if } t < t_c \tag{4.8a}$$

$$= q_u \quad \text{if } t \geq t_c \tag{4.8b}$$

t_c is construction time and q_u is ultimate load.

Upon the application of load, the *initial excess pore water pressure* (u_0) is generated uniformly within the clay layer. Fig. 4.1a shows the schematic representation of the chosen problem. The flow is assumed to be nonlinear (Fig. 4.9a) with stress-dependent permeability (Fig. 4.1b). The load application program is shown in Fig 4.9b. With the advancement of time, the pore fluid comes out of the sample resulting in the non-linear dissipation of the *excess pore water pressure* (PWP). Due to the incompressibility of the soil solids and fluids, the compression of the soil skeleton occurs solely because of the expulsion of pore water. The compression of the soil stratum and the fluid flow field occurs only along the direction of load application, which is vertical (z-axis). Throughout the process of consolidation, the soil remains to be saturated. The fluid properties are assumed to be unaffected by the change in temperature, viscosity, or density. It is intended to study the combined effect of non-Darcian flow, stress-dependent flow characteristics, compressibility characteristics, and ramp loading on the one-dimensional consolidation of the clayey layer. An uncoupled numerical analysis is performed without considering the creep effect and large deformation.

4.3.1.1 Non-linear flow Model and Stress-Dependent Characteristics

The fluid flow follows the Elnaggar et al. (1973)'s exponential equation, as under:

$$v = k_u \left(i - (1-a) i_1 \left[1 - \exp\left(\frac{-i\theta}{i_1} \right) \right] \right) \tag{4.9}$$

Here, (i) v=discharge velocity, (ii) a, θ, (empirical parameters) and i_1 (absolute threshold gradient) are the model parameters, and (iii) i=hydraulic gradient. Eq. 4.9 reduces to Darcian law if a=1, if θ= 0, or if i_1=0. Fig. 4.9a shows the v–i relationship (in the inset) indicating the minimum (k_m) and the maximum/ultimate (k_u) slopes (permeability) which are related as: $k_m = k_u[1-(1-a)\theta]$. The normalized variations of k_m (k_m/k_u) with respect to the model parameters are shown in Fig. 4.9a. The deviation from the Darcian flow increases for higher θ and lower a. The advantage of choosing Elnaggar et al. (1973)'s model is the flexibility of using the single equation without any constraint of establishing the C^0 and C^1 continuity, as in the case of other non-Darcian models (e.g. Hansbo 1960). The influence of the non-Darcian model parameters are shown in Fig. 4.10. The curves are drawn for different model parameters pertaining to two different ultimate permeability. Since permeability varies with space and time; therefore, the flow curve for every location is unique and changes with time.

4.3.2 Formulations and Solution Strategy

To formulate the 1-D diffusion equation, Elnaggar et al.'s nonlinear flow relationship is considered instead of Darcy's law. The other four relationships remain the same as in the previous section and include: (a) the continuity equation, (b) a compressibility-based stress-dependent permeability factor, (c) the non-zero divergence of the flow vector, and (d) the fundamental principle that the change in pore water pressure (u) equals the change in effective stress.

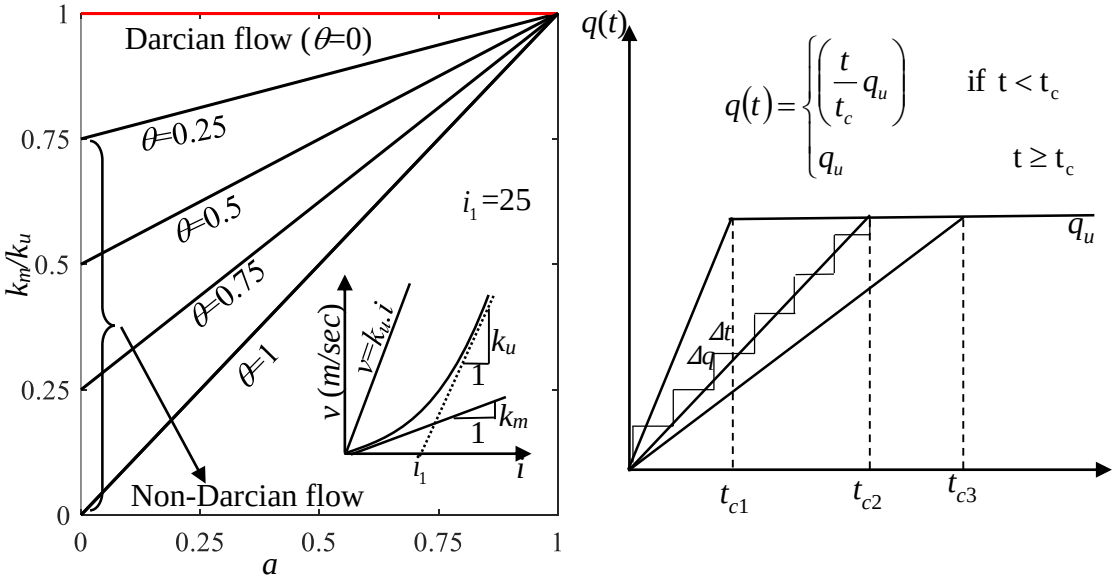

Fig. 4.9. (a) Impact of various non-Darcian flow model parameter on normalized minimum permeability (b) ramp loading,

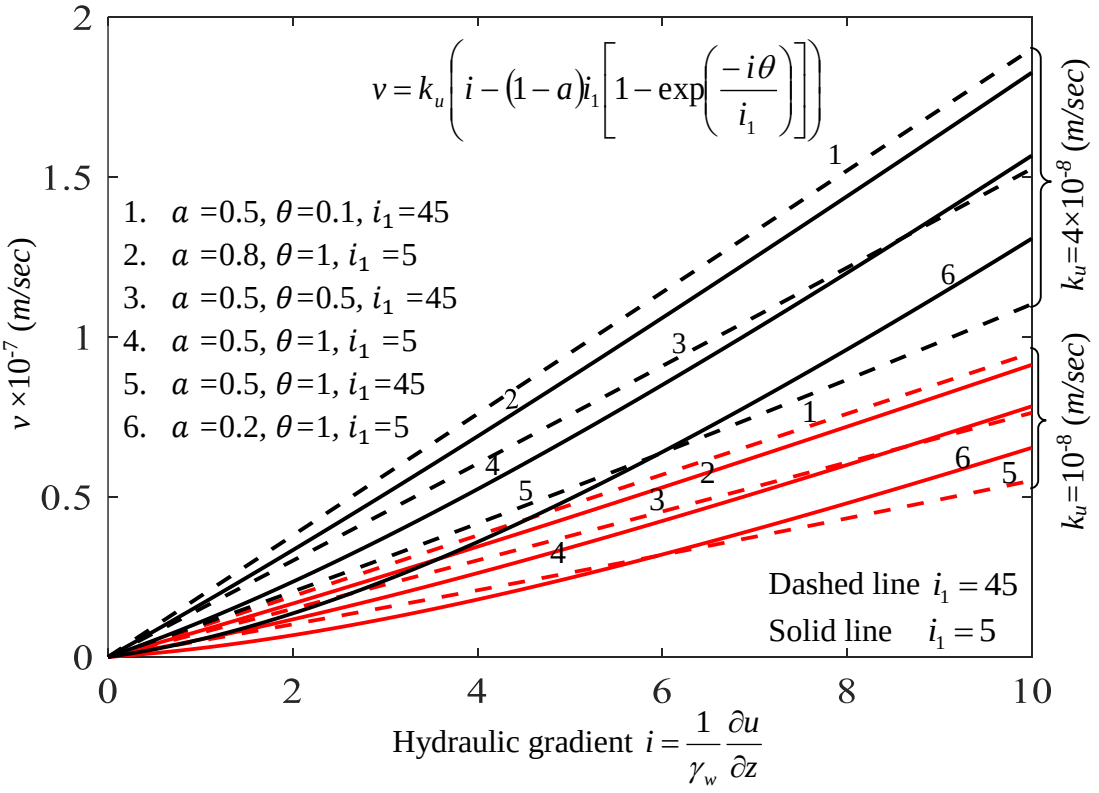

Fig. 4.10 The nonlinear variation of flow velocity with hydraulic gradient with the parameter variation and different permeability

The steps for determining the governing differential equations are cited in Appendix B3. Two different cases are considered during the development of the formulations. They are:

Case A: Where the permeability index (*M*) is finite and

Case B: Where *M* → infinity, i.e., constant permeability.

The parabolic partial differential equations (PDE) obtained for these two cases are written below:

$$\text{Case A}: X\frac{\partial^2 u}{\partial z^2}+Y\frac{\partial u}{\partial z}=\frac{\partial u}{\partial t}-\frac{\partial q}{\partial t} \tag{4.10}$$

$$\text{Where}\quad C_n=\frac{2.3(1+e_0)10^{\frac{A-B}{M}}}{C_c\gamma_w};\ X=C_n(\sigma')^{\beta}\cdot E;\ Y=C_n\gamma_w(1-\beta)(\sigma')^{\beta-1}\cdot E';$$

$$\beta=1-C_c/M\quad E=1-(1-a)\theta\left[\exp(-\theta i/i_1)\right]\ E'=i-(1-a)\theta i_1\left[1-\exp(-\theta i/i_1)\right]$$

$$X=\underbrace{2.3\sigma'(1+e_0)/(C_c\gamma_W)}_{\text{Compressibility Characteristics}}\cdot\underbrace{10^{(A-B)/M}(\sigma')^{\beta-1}}_{\text{Permeability Characteristics}}\cdot\underbrace{E}_{\text{non-Darcian Characteristics}} \tag{4.11}$$

$$\text{Case B}: X\frac{\partial^2 u}{\partial z^2}=\frac{\partial u}{\partial t}-\frac{\partial q}{\partial t} \tag{4.12}$$

$$M\to\infty\therefore\beta=1;\quad C_n=2.3(1+e_0)/(C_c\gamma_w),\qquad X=C_n\cdot\sigma'\cdot E$$

Same as the pervious section, the spatial derivatives (on the left-hand side) are equated with the temporal derivative on the right-hand side. Here the parameters *X* and *Y* consist of three terms: (a) constant term, C_n (which is a function of *A*, *B*, C_c, and *M*), (b) induced effective stress, and the additional (iii) non-Darcian model parameters. The dimensions of *X* and *Y* are L^2T^{-1} and LT^{-1}, respectively. Case B is a special case of the generalized Case A, wherein the permeability remains constant throughout the consolidation process. The equation representing Case B resembles the conventional dissipation equation ($c_v u''=\dot{u}$); the only difference is the coefficient (*X*) term. Unlike the c_v parameter (associated with the

conventional dissipation equation) the coefficient X is a function of effective stress and the non-Darcian parameters. Nevertheless, the term X in Case B is not influenced by (A, B, and M)-parameters but depends on σ'.

In essence, both compressibility and permeability are stress-dependent in Case A; however, the diffusion equation in Case B strictly pertains to constant permeability but stress-dependent compressibility. Cases A and B boil down to the conventional consolidation equation by imposing $X = c_v$, and Y=0. In this study, the parameters are considered in isolation for comprehending their individual impact. The boundary conditions are same as the previous section.

The Crank-Nicolson implicit scheme of the finite difference method is employed to solve the initial value problem (IVP), which is represented by the governing differential equation along with the boundary and the initial conditions. It is assumed that the applied incremental load instantaneously translated to the pore water pressure (PWP) uniformly within the entire consolidating domain. The domain in the vertical direction is discretized with equally-spaced n segments resulting in (n+1) number of grid points. For any arbitrary i^{th} grid point, the form of the discretized equation is as follows:

Case A
$$X_i^t\left[\frac{1}{2}\left\{\left.\frac{\partial^2 u}{\partial z^2}\right|_i^{t+\Delta t}+\left.\frac{\partial^2 u}{\partial z^2}\right|_i^{t}\right\}\right]+Y_i^t\left\{\left.\frac{\partial u}{\partial z}\right|_i^{t+\Delta t}\right\}=\left.\frac{\partial u}{\partial t}\right|_i-\left.\frac{\partial q}{\partial t}\right|_i \tag{4.13a}$$

Case B
$$X_i^t\left[\frac{1}{2}\left\{\left.\frac{\partial^2 u}{\partial z^2}\right|_i^{t+\Delta t}+\left.\frac{\partial^2 u}{\partial z^2}\right|_i^{t}\right\}\right]=\left.\frac{\partial u}{\partial t}\right|_i-\left.\frac{\partial q}{\partial t}\right|_i \tag{4.13b}$$

Appendix B4 shows the process of discretization and the algebraic equations obtained thereof. To linearize the nonlinear equations, the spatial gradient terms involved in X and Y are taken at the previous (known) time step. It is to be noted that the parameters L_i^t and P_i^t are dynamic variables and change with respect to time and space. Thus, the

equation can be converted into a simultaneous set of linear algebraic equations ($G^t \times U^{t+\Delta t} = H^t$). The equations are solved by employing the Gauss elimination technique.

Here at the preliminary stage, the homogenous compressible clays are first assigned with a uniform initial effective stress σ_0', distinct e–log$k$, e–logσ', and v–i no linear relationship. Hence, the input parameters are the same as the previous section with the additional non-Darcian model parameters (a, θ, i_1), and the features of the ramp load. The method of calculating k_0 and the subsequent method of calculating consolidation are the same as in the previous section. For Case B, a constant permeability (corresponding to e_0) is ascribed to all the nodes, throughout the consolidation. To model the ramp load, a small incremental load (dq) is applied over a very short time interval, dt, as illustrated in Fig. 4.9b. The unknown PWP vector (U) is updated by using: $U^{t+\Delta t} = U^t + dq * ones(n,1)$. The entire numerical program is developed in *MATLAB* (version 2018) tool.

4.3.3 Results and Discussions

After solving the IVP, the magnitude of excess PWP (u) is computed at each node corresponding to different time steps. The results are displayed in two different forms: (a) u-isochrones (the variation of u with depth at a specific time), and (b) consolidating curves (the variation of U_{avg} with respect to time). For the considered ramp loading, U_{avg} is calculated as:

$$U_{avg} = \begin{cases} \left(\dfrac{t}{t_c} - \dfrac{a_c}{q_0 H} \right) & \text{if } \; t < t_c \\ \left(1 - \dfrac{a_c}{q_0 H} \right) & \text{if } \; t \geq t_c \end{cases} \quad \begin{array}{l} a_c = \text{Area encompassed by the isochrone at time, } t \\ \quad = \displaystyle\int_0^H u(z,t)\,dz \end{array} \tag{4.14}$$

It is to be noted that the u-isochrones provide the spatial variation of u on a local scale and the consolidating curves, in a way, provide some sense of average settlement of the entire layer in a global perspective. A series of numerical simulations are performed to

understand how the consolidation of saturated clays gets influenced by the combined effect of the construction period, drainage boundaries, v–i, e–k and e–σ' relationships. Table 4.2 presents the chosen parameters (following Abbasi et al., 2007) and the variation of permeability and void ratio before and after the consolidation. The consolidating layer gets more compressed for a higher value of C_c and a lower value of A; nevertheless, the B and M parameters do not make any changes in the final compressibility. On the contrary, all the void ratio intercept and the slope parameters of the e–log$k$ and e–logσ' curves impress upon the permeability values.

Similar to the u-isochrones, new sets of permeability profiles (termed as k-isochrones) are drawn with depth. The k-isochrones reflect the spatial variation of permeability resulting from the effective stress increment with the advancement in the consolidation process. At any arbitrary space (z) and time (t), the permeability is evaluated by using Eq. 4.2 where the effective stress is expressed as:

$$\begin{aligned} \sigma'(z,t) &= \sigma'_0 && (t=0) \\ &= \sigma'_0 + q(t) - u(z,t) && (t < t_c) \\ &= \sigma'_0 + q_u - u(z,t) && (t \geq t_c) \\ &= \sigma'_0 + q_u && (t \to \infty) \end{aligned} \tag{4.15}$$

In the presented figures, a few symbols are used to indicate (i) loading-type (R=ramp loading, C=constant loading), (ii) flow-type (D=Darcian, ND=Non-Darcian), and (iii) the type of Cases (KV=Case A, K=Case B); for an example, RDK indicates the consolidation of the clay layer subjected to ramp loading, Darcian flow, and constant permeability case.

4.3.3.1 Effect of Model Parameters and Construction Time

Figs. 4.11 and 4.12 represent the consolidating curves for various non-Darcian model parameters and different construction times. Fig. 4.11 subscribes to the PTPB condition, while Fig. 4.12 adheres to the PTIB condition.

Table 4.2 Data used for the analysis

Input Parameters				$@t=0\ \ (\sigma'=\sigma'_0)$		$@t\to\infty(\sigma'=\sigma'_0+q_u)$		Differences			
A	B	C_c	M	k_0 (m/sec)	e_0	k_f (m/sec)	e_f	Δk	Δk in %	Δe	Δe in %
1.21	5.4	0.3	0.6	4.64×10^{-8}	1.00	1.01×10^{-8}	0.60	3.63×10^{-8}	78.23	0.40	40.00
1.21	5.4	0.5	0.6	2.72×10^{-8}	0.86	2.15×10^{-9}	0.20	2.51×10^{-8}	92.10	0.66	76.74
1.21	5.4	0.5	0.7	3.27×10^{-7}	0.86	3.72×10^{-8}	0.20	2.90×10^{-7}	88.62	0.66	76.74
1.50	5.4	0.3	0.6	1.42×10^{-7}	1.29	3.10×10^{-8}	0.89	1.11×10^{-7}	78.18	0.40	31.01
1.21	4.9	0.3	0.6	3.17×10^{-7}	1.00	4.71×10^{-8}	0.60	2.70×10^{-7}	85.14	0.40	40.00

Figs. 4.11a-4.11c and 4.12a-4.12c correspond to a specific set of θ (=0.5) and i_1 (=5) but for three different a values, namely, 0.2, 0.5, and 0.8. Figs. 4.11d-4.11f and 4.12d-4.12f correspond to a specific set of a (=0.5) and i_1 (=45) but for three different θ values, namely, 0.1, 0.5, and 1. Irrespective of the permeability characteristics, the Darcian law predicts a faster rate of consolidation than its non-Darcian counterpart. It is well observed that the deviation between Darcian and non-Darcian curves (denoted here as d_{nf}) grows significantly for the lower values of a and for higher values of θ. In the initial stage of consolidation, the magnitude of d_{nf} is almost negligible. Nevertheless, with the progress in consolidation, the deviation increases to a noticeable extent; this increment in d_{nf} is excessively higher for Case B than Case A. Moreover, the curves indicate that the θ-parameter has a more pronounced impact on the consolidation curve than the a- parameter. Evidently, for a =1 or θ=0, the non-Darcian curves coincide with the Darcian one. The parameter i_1 does not seem to impact the consolidation process significantly. Although the trend of the consolidating curves remains the same for both drainage conditions, however, there is almost a difference of two orders of magnitude in time for attaining the same percentage of consolidation.

Under constant loading, the consolidation curve remains smooth, while ramp loading causes a slight depression in the U_{avg} –t curves. The higher the t_c value, the depression occurs at a higher percentage of consolidation. In comparison to the ramp loading, the PWP dissipations occur faster for the constant loading. The influence of t_c on the consolidation behaviour appears to be substantial up to a certain percentage of consolidation; beyond that, the construction-time-induced deviations (termed here as d_{tc}) appear to be diminishing. In contrast to the constant permeability (Case B), the d_{tc} corresponding to the stress-dependent permeability (Case A) becomes zero with the advancement in the consolidation process. The coincidence of the U_{avg} –t curves occurs much earlier and more prominently for the PTIB drainage boundaries. For Case B with PTPB drainage boundaries, it is observed that the value of d_{tc} remains discernible even at a high degree of consolidation. For instance, corresponding to Case B with non-Darcian flow (a=0.2, θ=0.5, i_1=5), d_{tc} vanishes at 30% for PTIB, whereas, for PTPB, the presence of d_{tc} remains visible even at 80% consolidation. Similar to the constant loading, the increment of d_{nf} happens at the later stage of consolidation. The deviation of U_{avg} –t curves generated for Case B with conventional Darcian flow and Case A with non-linear flow is always greater under time-dependent ramp loading compared to constant loading.

The combined effects of drainage boundaries, loading type, flow types, and stress-dependent permeability are studied based on the percentage differences in consolidation (U_{avg}^{diff}) recorded at two specific times, namely, t_{40}^{RDK} and t_{80}^{RDK}, which are defined as the times pertaining to 40% and 80% consolidation of Case B soil-type subjected to ramp loading and Darcian flow. Tables 5.3 and 5.4 correspond to ramp and constant loading, respectively. Regardless of the loadings, drainage boundaries, and flow characteristics, the magnitude of U_{avg}^{diff} at 40% is substantially smaller than its counterpart value of U_{avg}^{diff} at 80%

consolidation for Case B soil type; however, for Case A soil, the increment of U_{avg}^{diff}, at 80% consolidation, is relatively marginal. For instance, conforming to PTPB condition, U_{avg}^{diff} between RDK and RNDK increases from 8.68% (at t_{40}^{RDK}) to 30.38% (at t_{80}^{RDK}) for the soil having C_c=0.3, M=0.6, A=1.21, and B=5.4; whereas, for the same soil U_{avg}^{diff} between RDKV and RNDKV increases from 5.79% (at t_{40}^{RDK}) to 8.66% (at t_{80}^{RDK}) only. It can be interpreted that flow law is highly influential for Case B than Case A. In addition to that, for Darcian flow, the U_{avg}^{diff} between Case A and Case B recorded at t_{80}^{RDK} is significantly higher than that of t_{40}^{RDK}; however, for non-Darcian flow, the enhancement of U_{avg}^{diff} at t_{80}^{RDK} is relatively smaller than that of t_{40}^{RDK}. It can be interpreted that the influence of effective stress on permeability is pivotal if the fluid flow obeys Darcian law. Furthermore, the magnitude of U_{avg}^{diff} seems to be higher for ramp loading than the constant loading type.

4.3.3.2 Effect of *A* and *B* Parameters on Permeability and Rate of Consolidation

Fig. 4.13 displays the influence of parameters *A* and *B* on the *k*-isochrones for PTPB and PTIB drainage boundaries corresponding to Darcian and non-Darcian flows and subjected to constant loading. By considering two different values of *A* (1.21 and 1.50) and *B* (4.9 and 5.4), the *k*-isochrones are drawn at two different times (For PTPB 30 and 45 days, for PTIB 30 and 180 days) corresponding to C_c=0.3, M=0.6. The figure reveals that the journey of *k*-isochrones lies between two lines of constant permeability (k_0 and k_f lines); the k_0-line corresponds to the instant of load application (t=0), *and the* k_f-line pertains to the end of consolidation (t=∞). Evidently, the permeability increases either with an increase in *A* or with a decrease in *B*. Owing to the form of the effective stress distributions during the consolidation, the *k*-isochrones appears to be (i) a bell-shaped parabolic curve (minimum at the end and maximum at the middle) for the PTPB condition, and (ii) a

sigmoid-shaped curve (minimum at the top maximum at the bottom) for the PTIB condition. In the initial stage of consolidation, the maximum variations in the *k*-isochrones between Darcian and non-Darcian curves (termed as $k_{D-ND}^{\max}$) occurs either at the adjacent of the drainage boundaries (for PTPB) or at the mid-portion (for PTIB) of the consolidating layer. Nevertheless, after a certain level of excess PWP dissipation, $k_{D-ND}^{\max}$ shifts and occurs at the (a) central portion (for PTPB), or (b) bottom boundary (for PTIB) of the clayey layer.

Fig. 4.14 illustrates the influence of *A* and *B* parameters on the consolidation curves for constant and ramp loading corresponding to both drainage boundaries. The figure depicts that the rate of consolidation accelerates with the increase in *A* as well as with the decrease in *B*. Besides that, ramp loading causes higher d_{nf} for larger B and smaller A. The figure also gives an impression that the rate of consolidation is significantly influenced by the *B* parameters as compared to the *A* parameter, across all the applied loadings and drainage boundaries; this feature can also be explained by the *k*-isochrones as shown in Fig.4.13. From Tables 4.3 and 4.4, it can be observed that with the increase in *A* (or decrease in *B*), the value of U_{avg}^{diff} at t_{40}^{RDK} between Cases A and B gets enhanced if the flow is Darcian; but shows reverse characteristics for non-Darcian flow.

4.3.3.3 Effect of *M* and C_c Parameters on Permeability and Rate of Consolidation

Fig. 4.15 displays the impact of *M* and C_c on the *k*-isochrones; Figs. 4.15a and 4.15b correspond to PTPB and Figs. 4.15c and 4.15d pertain to PTIB drainage boundaries. With an increase in C_c and a decrease in *M*, the percentage range between k_0 and k_f widens up, however, the initial and final values of permeability decreases. As the drainage boundaries are considered to be extreme, therefore completely drained boundary results in an instantaneous change of permeability from k_0 to k_f, whereas, the condition of a fully impervious boundary ensures an orthogonal intersection of *k*-isochrones with the undrained boundary.

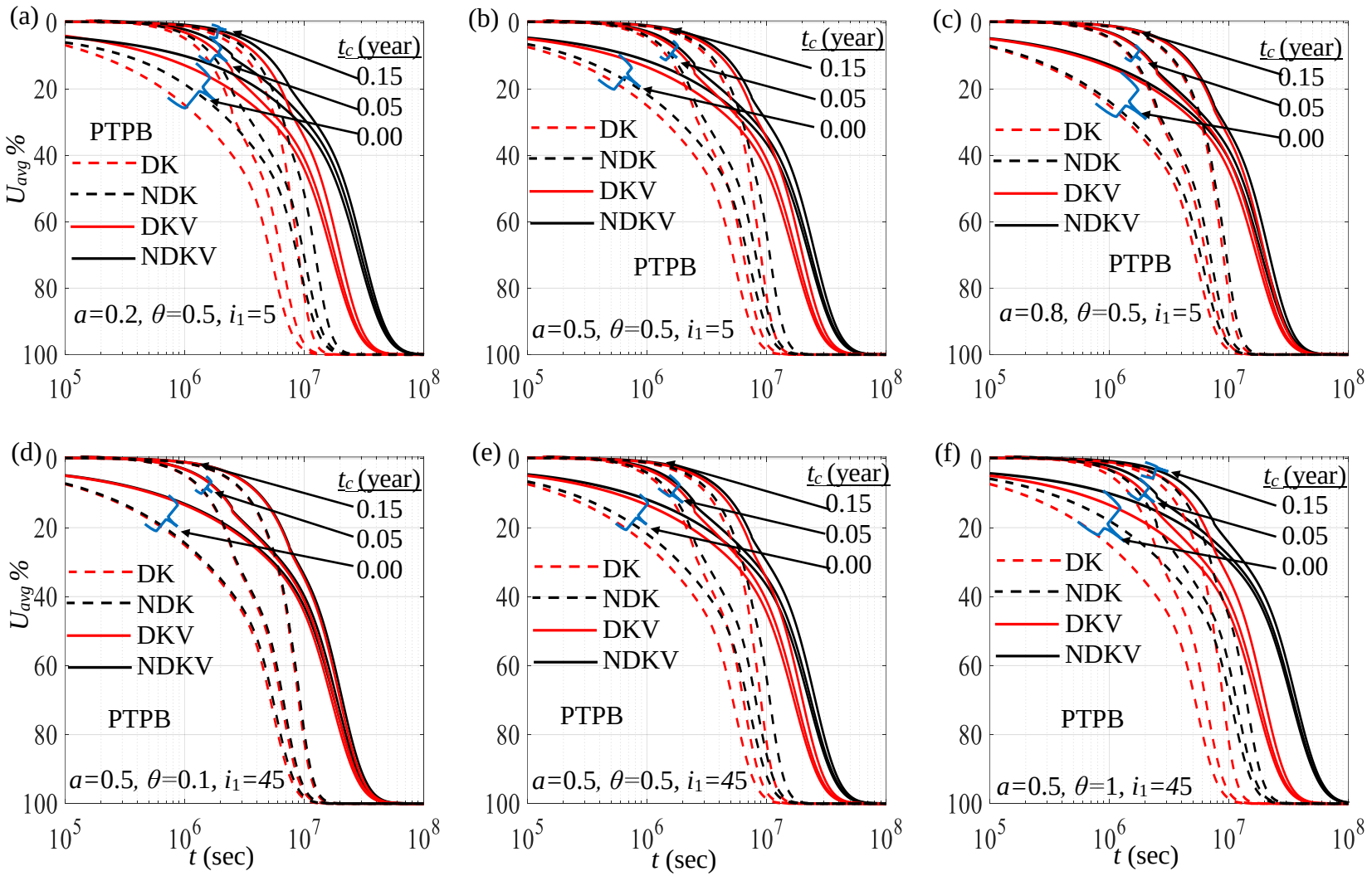

Fig 4.11 Consolidating curves for PTPB at three different construction time (t_c), namely 0.0, 0.05, and 0.15 that corresponds to various model parameters.

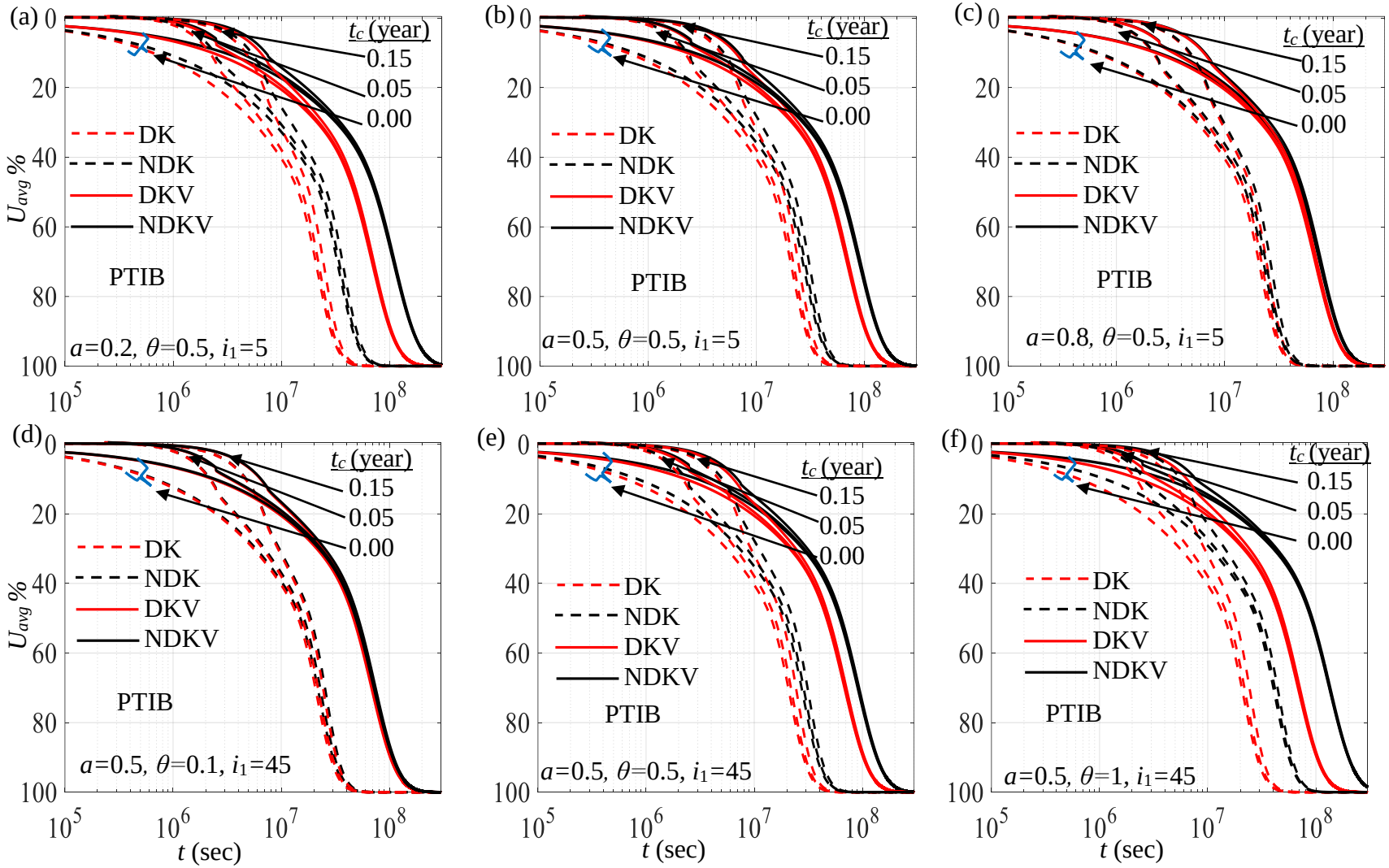

Fig. 4.12 Consolidating curves for PTIB at three different construction time (t_c), namely 0.0, 0.05, and 0.15 that corresponds to various model parameters.

At the initial stage of consolidation, the *k*-isochrone for PTIB overlaps with the k_0 lines adjacent to the bottom undrained boundary; the extent of this overlapping spreads a higher zone for lower C_c and higher *M*. With the progress in consolidation, the permeability at the impervious boundary reduces and advances towards k_f value. The curves are drawn for Darcian as well as non-Darcian flow. In comparison to C_c, variation of *M* appears to be more influential on the d_{nf} values. Barring the initial stage of consolidation, the d_{nf} happens to be the maximum either at the mid-portion of the clayey layer (for PTPB) or at the bottom undrained boundary (for PTIB). The impacts of the slope parameters (C_c and *M*) on the consolidation curves are illustrated in Fig. 4.16; the curves are plotted for both the drainage boundaries with different loading rates (t_c=0 and 0.05) and the constant *e*-intercepts (*A*=3, *B*=5). The rate of consolidation increases with an increase in *M* as well as a decrease in C_c; however, *M* appears to be more influential than C_c. The deviation in the U_{avg} vs. *t* curves generated from Case A and Case B grows remarkably with the decrease in the *M* parameter. Irrespective of the flow laws, drainage boundaries, and applied load type, the U_{avg}^{diff} (reported at t_{40}^{RDK} and t_{80}^{RDK}) between Case A and Case B enhances with the increase in *M* or a decrease in C_c. Furthermore, the effect of *M* and C_c parameters on the rate of consolidation appears to be more effective when the clayey layer is under ramp loading as opposed to the constant loading.

4.3.3.4 Effect of Various Parameters on the *u*-Isochrones

Figs. 4.17 and 4.18 display the combined effect of the slope parameters (C_c, *M*), drainage boundaries, flow laws, analyses-type (Case A and Case B), and the loading type on the conventional *u*-isochrones. It can be inferred that during the consolidation, the maximum PWP happens to occur at the portion where the permeability is maximum. The PWP dissipation happens to be quite rapid for Case B analysis. A slight alteration in the *M* parameter (say 0.6 to 0.7) makes a huge change in the PWP-dissipation profiles; the higher the *M* faster the

Table 4.3 Variation between various cases due to changes in state parameters for ramp loading under PTPB and PTIB conditions

Soil properties	Cases	PTPB		PTIB	
		at 40% of RDK	at 80% of RDK	at 40% of RDK	at 80% of RDK
	RDK-RDKV	17.65	46.59	19.90	49.76
Cc=0.3	RDK-RNDK	8.68	30.38	10.54	34.54
M=0.6	RDK-RNDKV	23.44	55.27	25.17	57.07
A=1.21	RDKV-RNDK	-8.97	-16.20	-9.37	-15.22
B=5.4	RDKV-RNDKV	5.79	8.68	5.27	7.32
	RNDK-RNDKV	14.76	24.88	14.63	22.54
	RDK-RDKV	26.33	59.03	26.93	60.00
Cc=0.5	RDK-RNDK	10.42	32.41	11.12	32.78
M=0.6	RDK-RNDKV	29.80	63.66	30.73	64.39
A=1.21	RDKV-RNDK	-15.91	-26.62	-15.80	-27.22
B=5.4	RDKV-RNDKV	3.47	4.63	3.80	4.39
	RNDK-RNDKV	19.39	31.25	19.61	31.61
	RDK-RDKV	22.86	52.66	24.00	55.90
Cc=0.5	RDK-RNDK	10.71	29.51	9.07	32.78
M=0.7	RDK-RNDKV	26.91	59.61	27.80	62.05
A=1.21	RDKV-RNDK	-12.15	-23.15	-14.93	-23.12
B=5.4	RDKV-RNDKV	4.05	6.94	3.80	6.15
	RNDK-RNDKV	16.20	30.09	18.73	29.27
	RDK-RDKV	19.67	46.38	19.35	47.66
Cc=0.3	RDK-RNDK	11.90	32.05	9.92	32.90
M=0.6	RDK-RNDKV	24.28	54.63	24.68	55.16
A=1.5	RDKV-RNDK	-7.77	-14.33	-9.44	-14.76
B=5.4	RDKV-RNDKV	4.61	8.26	5.32	7.50
	RNDK-RNDKV	12.38	22.58	14.76	22.26
	RDK-RDKV	20.40	46.86	17.18	47.18
Cc=0.3	RDK-RNDK	14.57	32.54	9.68	32.18
M=0.6	RDK-RNDKV	25.25	58.03	23.23	54.92
A=1.21	RDKV-RNDK	-5.83	-14.33	-7.50	-15.00
B=4.9	RDKV-RNDKV	4.86	11.17	6.05	7.74
	RNDK-RNDKV	10.68	25.50	13.55	22.74

Table 4.4 Variation between various cases due to changes in state parameters for constant loading under PTPB and PTIB conditions

Soil properties	Name	PTPB		PTIB	
		at 40% of RDK	at 80% of RDK	at 40% of RDK	at 80% of RDK
Cc=0.3 *M*=0.6 *A*=1.21 *B*=5.4	CDK-CDKV	17.18	45.15	17.32	46.22
	CDK-CNDK	8.74	33.20	8.78	32.32
	CDK-CNDKV	21.84	53.01	21.71	53.17
	CDKV-CNDK	-8.45	-11.94	-8.54	-13.90
	CDKV-CNDKV	4.66	7.86	4.39	6.95
	CNDK-CNDKV	13.11	19.81	12.93	20.85
Cc=0.5 *M*=0.6 *A*=1.21 *B*=5.4	CDK-CDKV	22.72	54.47	22.44	55.12
	CDK-CNDK	9.32	30.58	9.02	30.49
	CDK-CNDKV	26.21	59.71	25.85	59.76
	CDKV-CNDK	-13.40	-23.88	-13.41	-24.63
	CDKV-CNDKV	3.50	5.24	3.41	4.63
	CNDK-CNDKV	16.89	29.13	16.83	29.27
Cc=0.5 *M*=0.7 *A*=1.21 *B*=5.4	CDK-CDKV	20.97	52.43	21.46	52.44
	CDK-CNDK	9.32	32.04	9.27	29.88
	CDK-CNDKV	24.76	58.54	25.12	58.29
	CDKV-CNDK	-11.65	-20.39	-12.20	-22.56
	CDKV-CNDKV	3.79	6.12	3.66	5.85
	CNDK-CNDKV	15.44	26.50	15.85	28.41
Cc=0.3 *M*=0.6 *A*=1.5 *B*=5.4	CDK-CDKV	16.39	44.20	18.29	44.76
	CDK-CNDK	8.78	29.27	9.51	28.78
	CDK-CNDKV	21.66	51.95	22.20	51.95
	CDKV-CNDK	-7.61	-14.93	-8.78	-15.98
	CDKV-CNDKV	5.27	7.76	3.90	7.20
	CNDK-CNDKV	12.88	22.68	12.68	23.17
Cc=0.3 *M*=0.6 *A*=1.21 *B*=4.9	CDK-CDKV	17.56	43.61	16.83	46.59
	CDK-CNDK	9.66	28.68	8.54	33.90
	CDK-CNDKV	21.95	51.80	21.95	53.41
	CDKV-CNDK	-7.90	-14.93	-8.29	-12.68
	CDKV-CNDKV	4.39	8.20	5.12	6.83
	CNDK-CNDKV	12.29	23.12	13.41	19.51

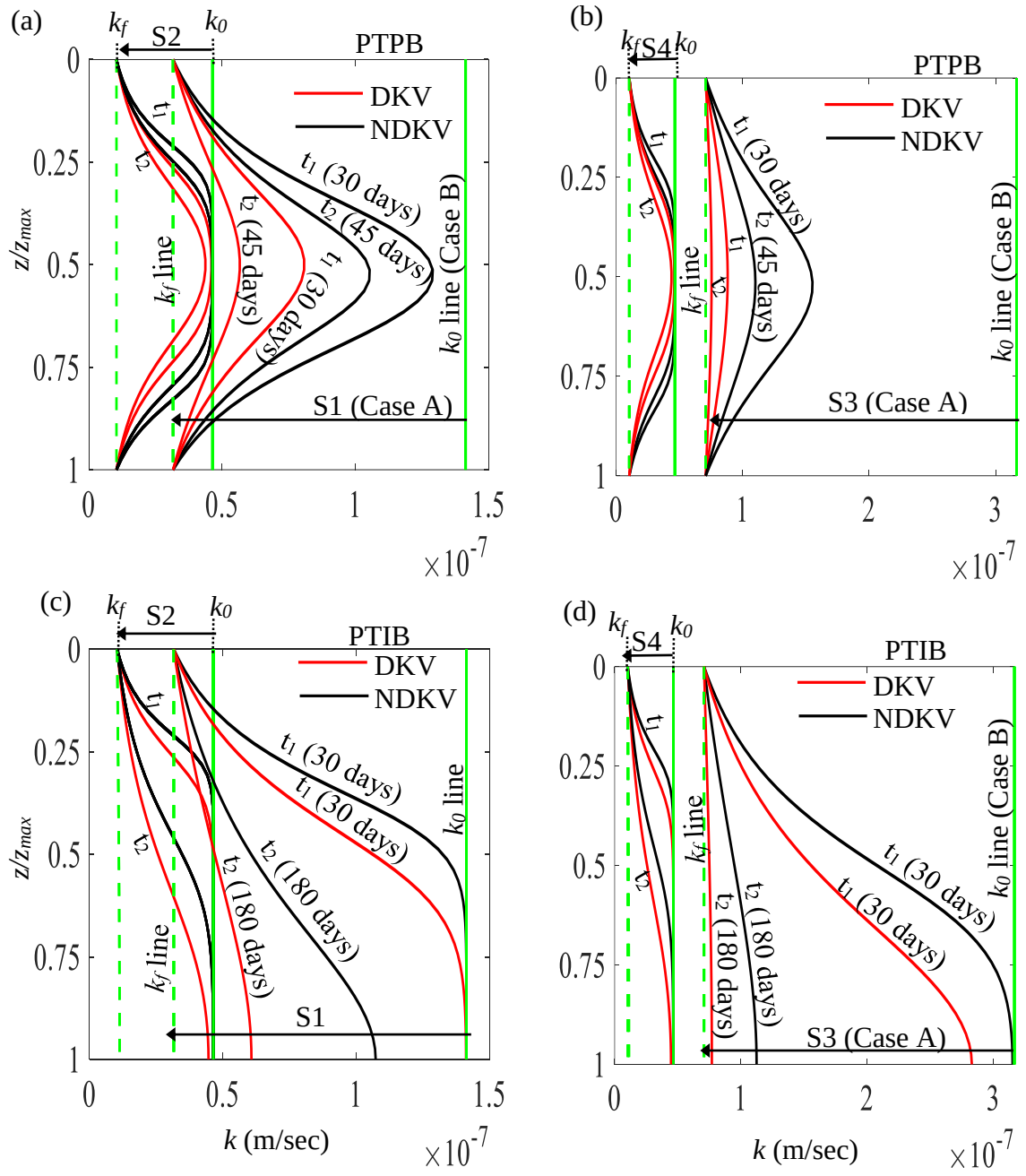

Constant parameters for Soil		*e*-intercepts(Variables)			
ND Flow	a=0.2, θ=0.5, i_1=10	S1	S2	S2	S2
Rates	C_c=0.3, M=0.5	A=1.5,B=5.4	A=1.21,B=5.4	A=1.21,B=4.9	A=1.21B=5.4

Fig. 4.13 *k*-isochrones graph for (a) *A* variation in PTPB (b) *B* variation IN PTPB (c) *A* variation in PTIB (d) *B* variation in PTIB

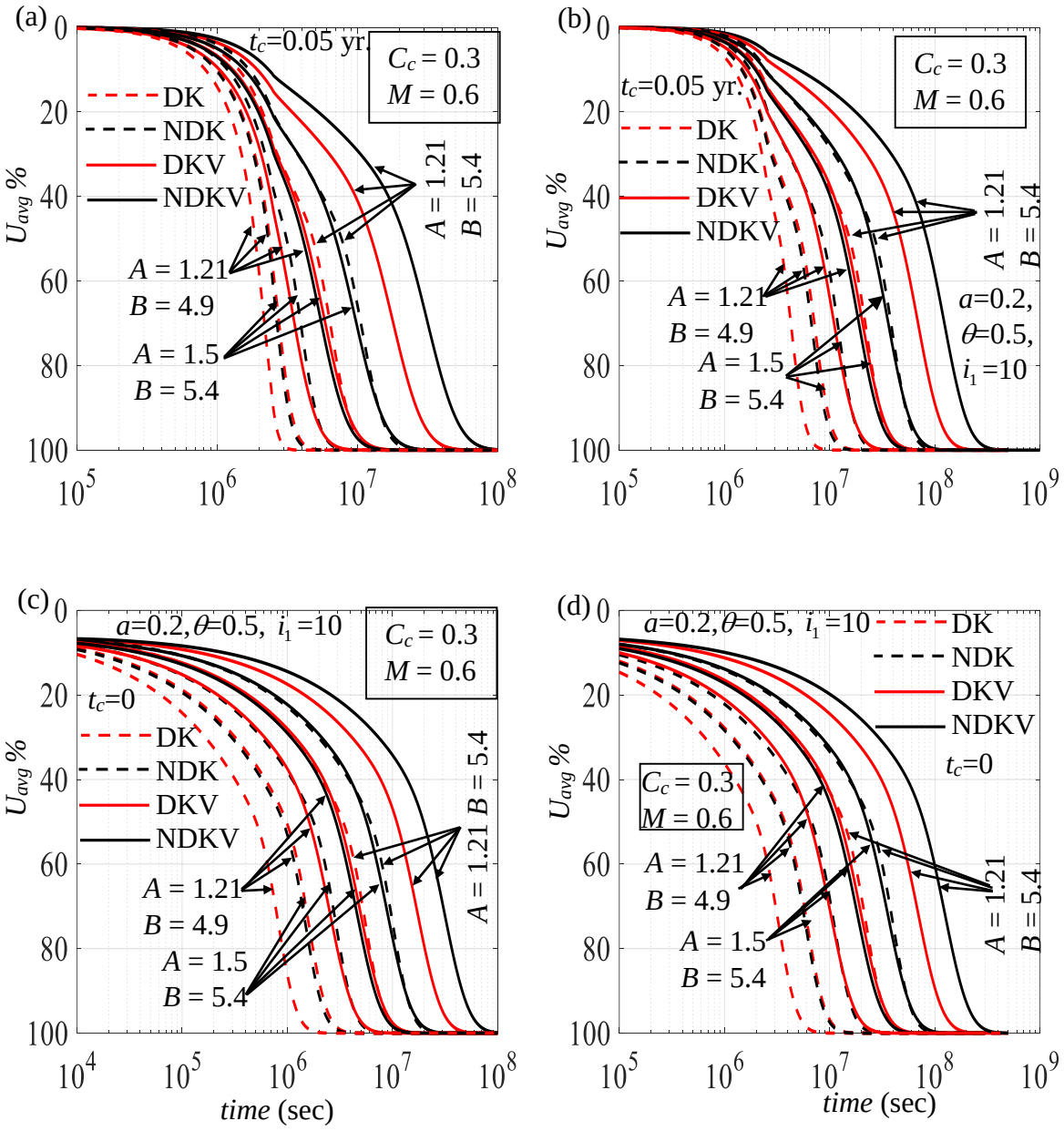

Fig. 4.14 Consolidation curve depicting variation of C_c and M in (a) ramp loading PTPB (b) ramp loading PTIB (c) constant loading in PTPB (d) constant load in PTIB

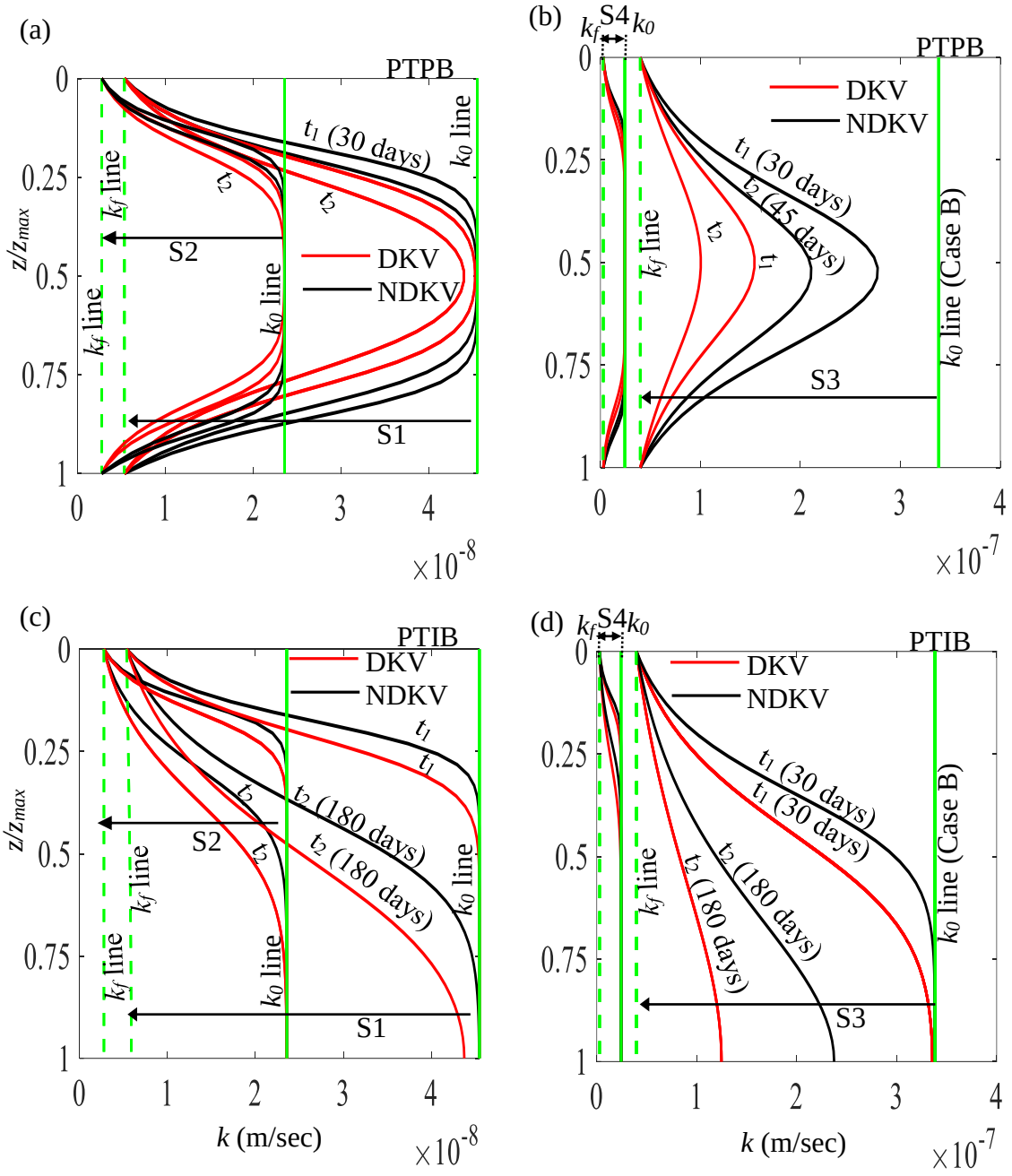

Constant parameters for Soil		Rates (Variables)			
e-intercepts	A=1.21,B=5.4	S1	S2	S3	S4
ND flow	a=0.2,θ=0.5, i_T =10	C_c=0.3,M=0.6	C_c=0.5,M=0.6	C_c=0.5,M=0.7	C_c=0.5,M=0.6

Fig. 4.15 *k*-isochrones graph for (a) C_c variation in PTPB (b) M variation IN PTPB (c) C_c variation in PTIB (d) M variation IN PTIB

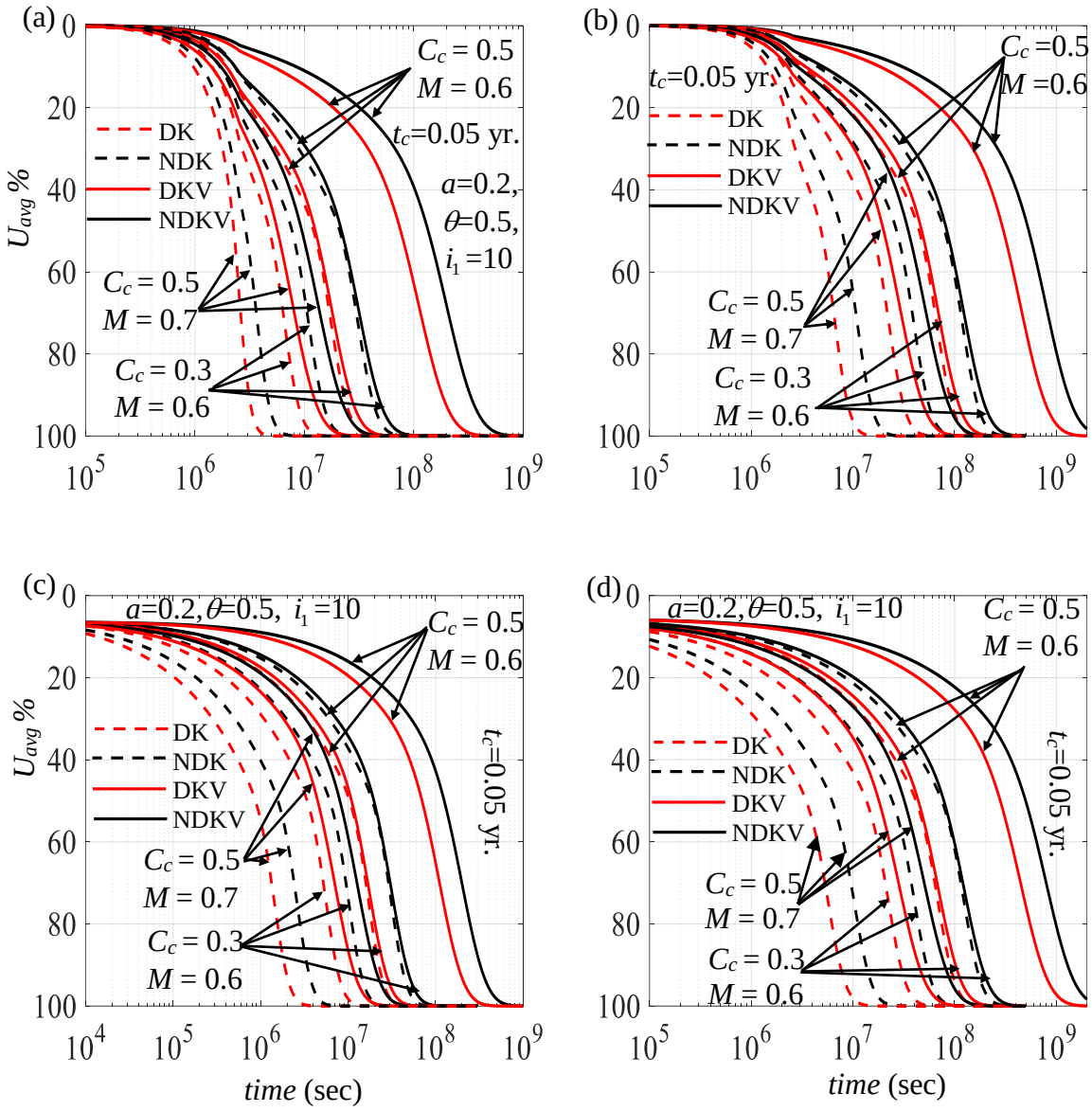

Fig. 4.16 Consolidation curve depicting variation of C_c and M in (a) ramp loading PTPB (b) ramp loading PTIB (c) constant loading in PTPB (d) constant load in PTIB

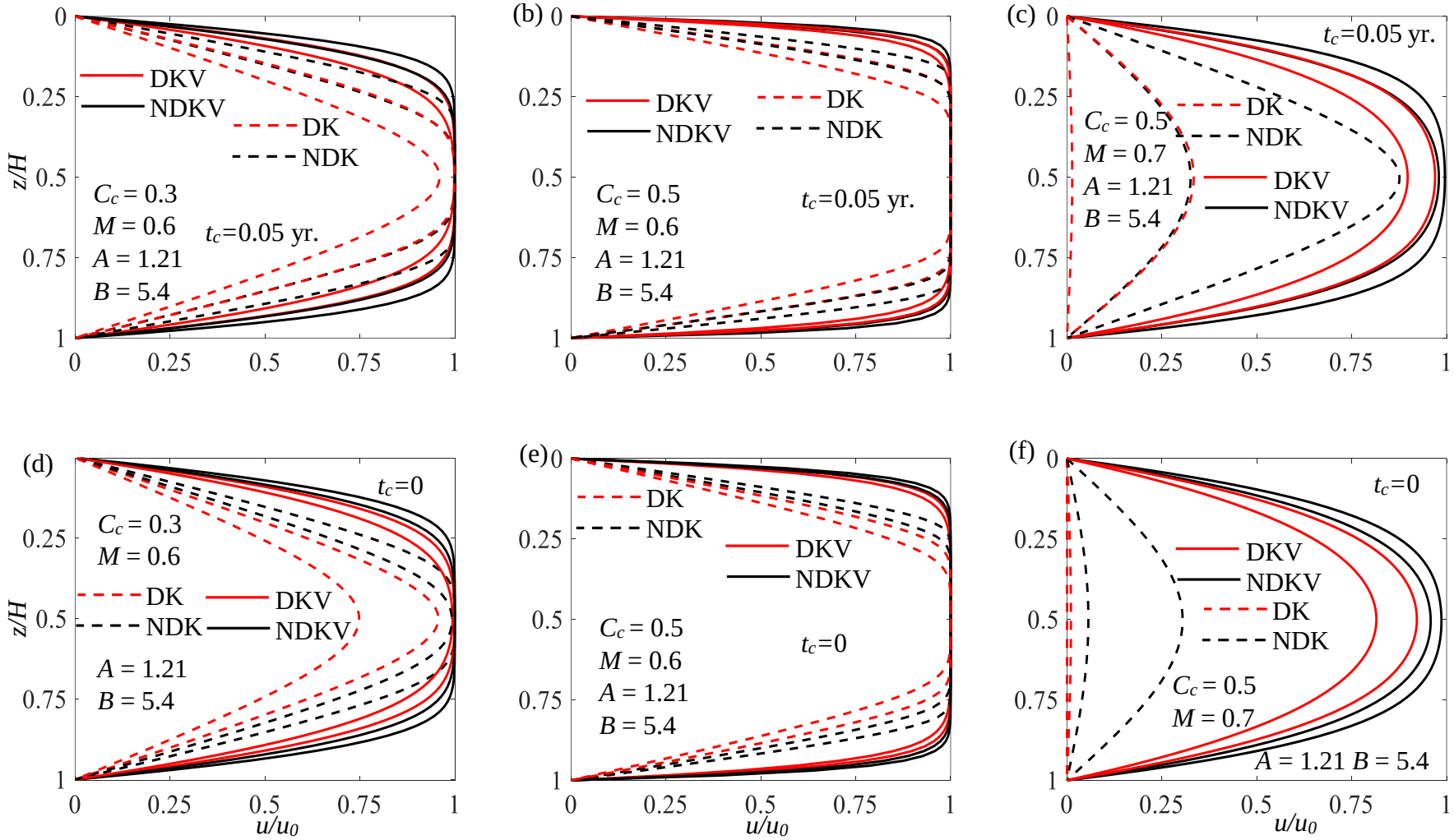

Fig. 4.17 Isochrones for Ramp (t_c = 0.05) and constant load (t_c = 0) in PTPB at time 30days and 45days with C_c and M variations

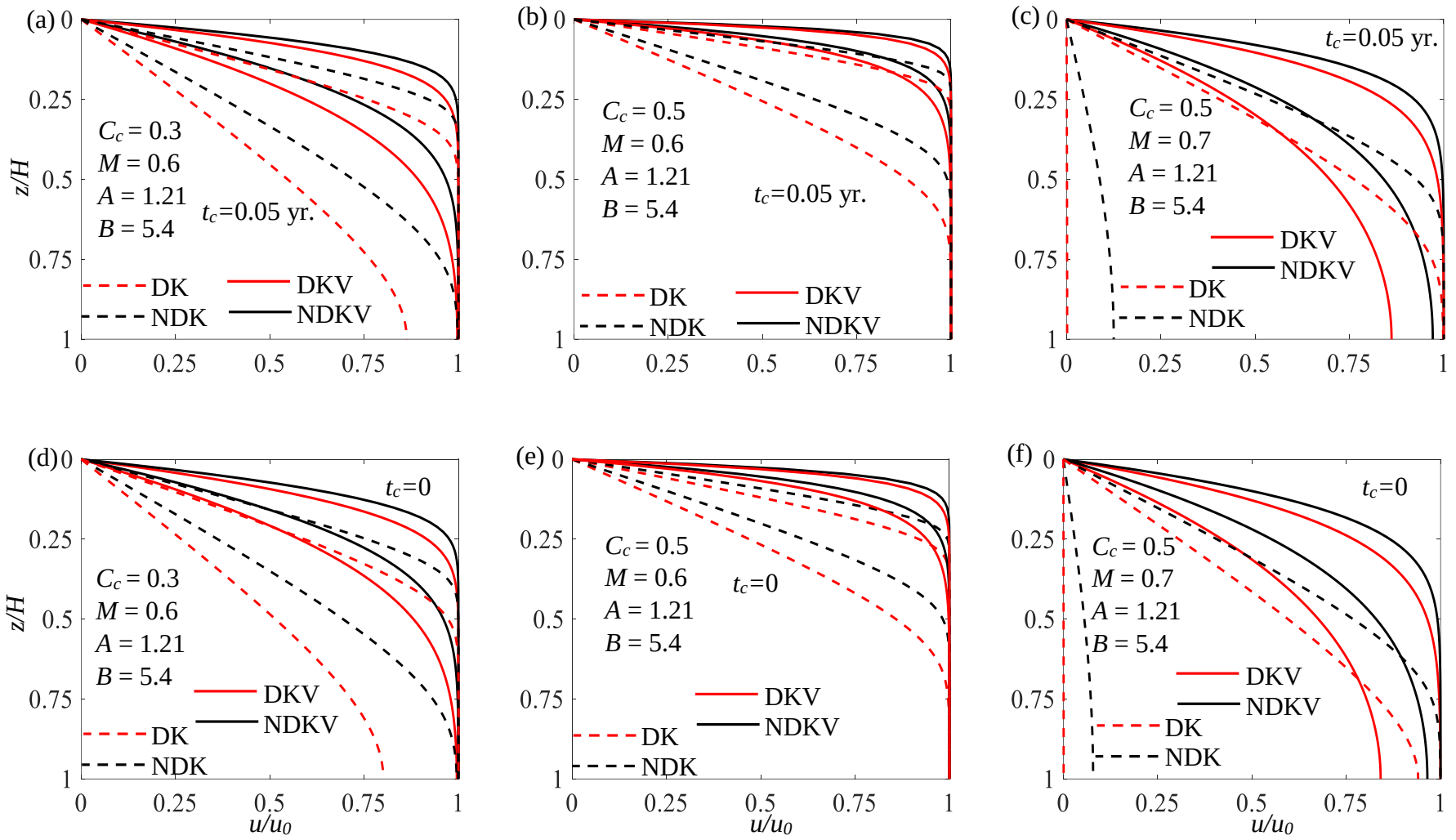

Fig. 4.18 Isochrones for Ramp ($t_c = 0.05$) and constant load ($t_c = 0$) in PTIB at time 30 days and 180 days with C_c and M variation

dissipation. The *u*-isochrones also corroborate the previous finding that the ramp loading delays the process of consolidation. The Darcian flow-based *u*-isochrones encompass less amount of the remaining PWP area than its non-Darcian counterpart. The distinction between Darcian and non-Darcian flow expands with time and is more pronounced for higher M or lower C_c. Furthermore, the difference between the *u*-isochrones generated from the two flow laws becomes more appreciable for the PTPB condition.

4.4 VALIDATION OF RESULTS

The present solution was compared for the quasi-permeability by Abbasi et al. (2007), Li et al. (2018) and Xie et al. (2012). Figure 4.19a demonstrates that the current solution closely aligns with the results presented by Abbasi et al. (2007), who used the Finite Difference Method (FDM) for consolidation with variable permeability and compressibility under Darcian flow and constant loading. Figures 4.19b and 4.19c illustrate analyses conducted using the analytical solution by Li et al. (2018) for non-linear consolidation with variable permeability under ramp loading. The curves indicate that the present analysis agrees well with both ramp loading and non-linear consolidation. Additionally, the results validate the non-Darcian analysis performed by Xie et al. (2012) using Terzaghi's consolidation theory. Figures 4.19d and 4.19e show that the present analysis is in good agreement with Xie et al. (2012) for non-Darcian flow. The results coincide with a variation of less than 0.01%. The analysis and results match well with the reported data, with a deviation between 5-10%. This deviation can be attributed to differences in the techniques used for the analysis.

4.5 SUMMARY

This chapter primarily focuses on investigating the effect of stress-dependent permeability and compressibility on the consolidation of homogenous and isotropic clays.

	Sample 1	Sample 2	Sample 3
σ_0' (kPa)	15	60	60
A	2.77	1.36	1.10
C_c	0.61	0.33	0.24
B	8.10	2.71	1.70
M	0.92	0.29	0.15

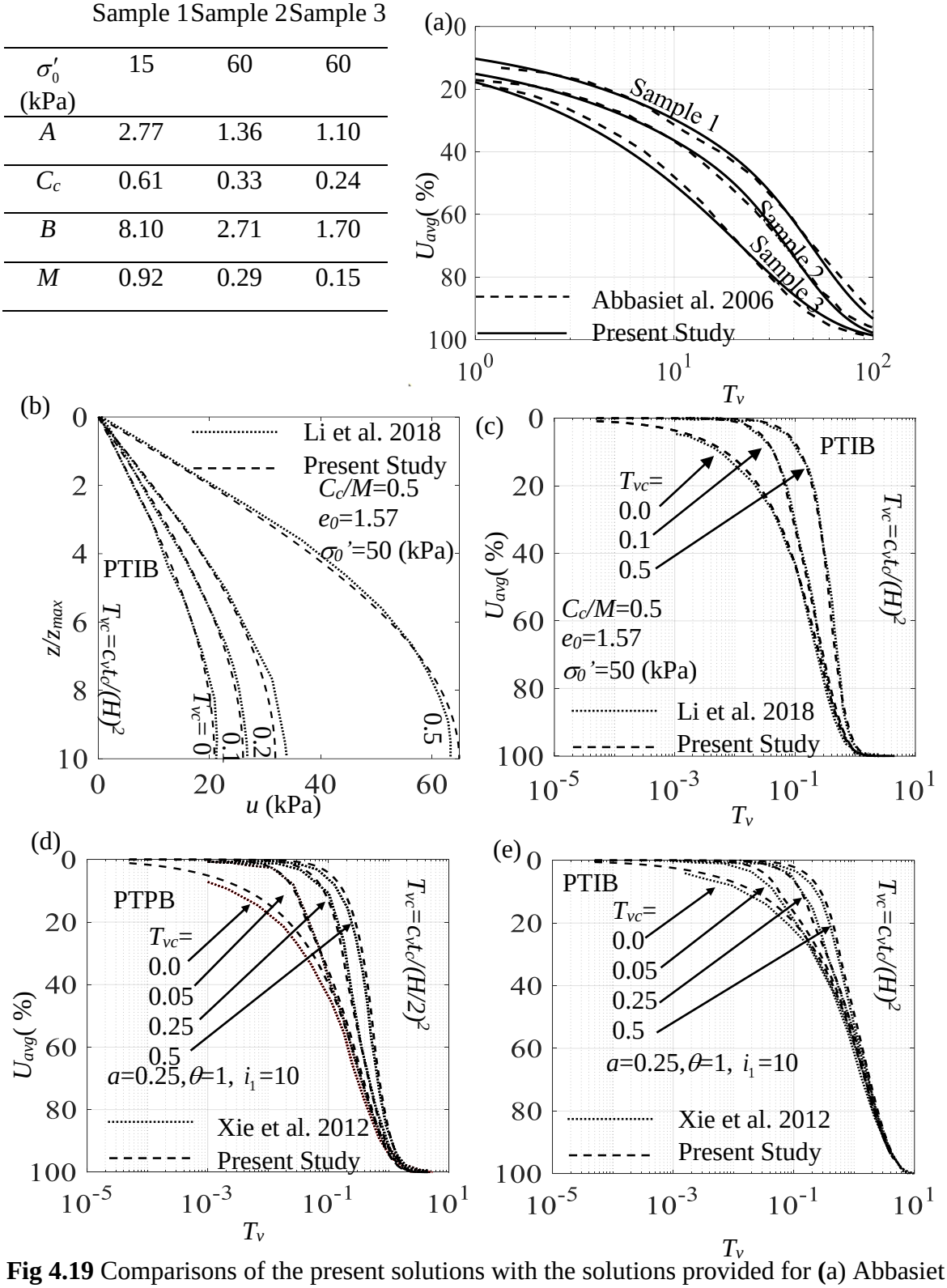

Fig 4.19 Comparisons of the present solutions with the solutions provided for **(**a) Abbasiet al. 2006, **(**b) and (c) Li et al. 2018, (d) and (e) Xie et al. 2012

In the first part of this chapter, the conventional quasi-permeability variation is verified with the total permeability variation. When dealing with quasi-permeability variation, the temporal derivative of u corresponds to the second-order spatial derivative of u; however, for total-permeability variation, it corresponds to both the second-order and first-order spatial derivatives of u. The spatial derivative terms are associated with the stress-dependent coefficients. In the second part, the total permeability variation is combined with the exponential and threshold gradient-based non-Darcian flow and time-dependent ramp loading. The numerical investigation is performed by employing the Crank-Nicolson implicit method of the finite difference scheme. The simulations are performed for the single as well as double drainage layer. The results are presented in terms of normalized isochrones, consolidating curves, and PWP profiles. A detailed investigation is done to examine the impact of various parameters: (a) void ratio-intercept of the *e-log*σ' and *e-logk* curves, (b) compressibility and permeability indices, (c) non-darcian flow parameters (a, θ and i_1), and (d) construction time (t_c). The results elucidate the effects of stress-induced nonlinear material properties and fluid flow on the consolidation subjected to ramp loading.